Inorganic Chemistry

pubs.acs.org/IC Article

Cytotoxic Ruthenium(II) Complexes of Pyrazolylbenzimidazole Ligands That Inhibit VEGFR2 Phosphorylation

Ayan Chakraborty,[†] Souryadip Roy,[†] Manas Pratim Chakraborty, Shantanu Saha Roy, Kallol Purkait, Tuhin Subhra Koley, Rahul Das, Moulinath Acharya, and Arindam Mukherjee*

Cite This: *Inorg. Chem.* 2021, 60, 18379−18394 Read Online

ACCESS | Metrics & More | Article Recommendations | Supporting Information

ABSTRACT: Eight new ruthenium(II) complexes of *N*,*N*-chelating pyrazolylbenzimidazole ligands of the general formula $[Ru^{II}(p\text{-cym})(L)\text{-}X]^+$ [where the ligand L is 2-(1*H*-pyrazol-1-yl)-1*H*-benzo[*d*]imidazole (**L1**) substituted at the 4 position of the pyrazole ring by Cl (**L2**), Br (**L3**), or I (**L4**) and X = Cl^- and I^-] were synthesized and characterized using various analytical techniques. Complexes **1** and **3** were also characterized by single-crystal X-ray crystallography, and they crystallized as a monoclinic crystal system in space groups $P2_1/n$ and $P2_1/c$, respectively. The complexes display good solution stability at physiological pH 7.4. The iodido-coordinated pyrazolylbenzimidazole ruthenium(II) *p*-cymene complexes (**2**, **4**, **6**, and **8**) are more resistant toward hydrolysis and have less tendency to form monoaquated complexes in comparison to their chlorido analogues (**1**, **3**, **5**, and **7**). The halido-substituted 2-(1*H*-pyrazol-1-yl)-1*H*-benzo[*d*]imidazole ligands, designed as organic-directing molecules, inhibit vascular endothelial growth factor receptor 2 (VEGFR2) phosphorylation. In addition, the ruthenium(II) complexes display a potential to bind to DNA bases. The cytotoxicity profile of the complexes (IC_{50} ca. 9−12 μM for **4**−**8**) against the triple-negative breast cancer cells (MDA-MB-231) show that most of the complexes are efficient. The lipophilicity and cellular accumulation data of the complexes show a good correlation with the cytotoxicity profile of **1**−**8**. The representative complexes **3** and **7** demonstrate the capability of arresting the cell cycle in the G2/M phase and induce apoptosis. The inhibition of VEGFR2 phosphorylation with the representative ligands **L2** and **L4** and the corresponding metal complexes **3** and **7** *in vitro* shows that the organic-directing ligands and their complexes inhibit VEGFR2 phosphorylation. Besides, **L2**, **L4**, **3**, and **7** inhibit the phosphorylation of extracellular signal-regulated kinase 1/2 (ERK1/2) and proto-oncogene tyrosine-protein kinase (Src), capable of acting downstream of VEGFR2 as well as independently. Compounds **L2**, **L4**, **3**, and **7** have a lesser effect on ERK1/2 and more prominently affect Src phosphorylation. We extended the study for **L2** and **3** in the Tg(fli1:gfp) zebrafish model and found that **L2** is more effective *in vivo* compared to **3** in inhibiting angiogenesis.

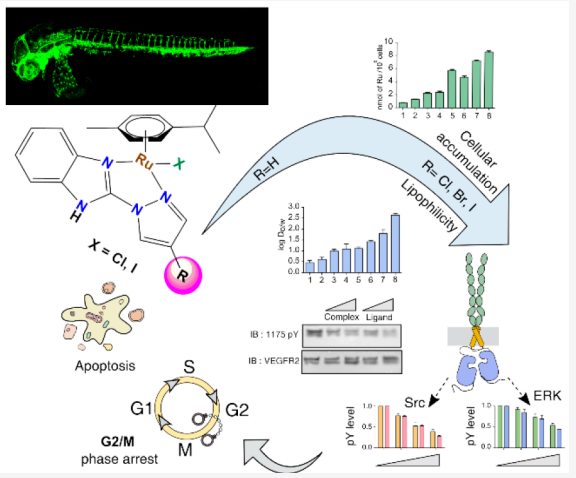

Downloaded via TSINGHUA UNIV on November 4, 2022 at 00:47:54 (UTC).
See https://pubs.acs.org/sharingguidelines for options on how to legitimately share published articles.

INTRODUCTION

Metal complexes have occupied an important place in cancer chemotherapy, helping to cure or prolong millions of lives.[1] This domination is solely led by the success of platinum(II) (Pt^{II}) drugs against various forms of cancer.[1−4] Apart from Pt complexes, ruthenium(II/III) ($Ru^{II/III}$), gallium(III) (Ga^{III}), and palladium(II) (Pd^{II}) complexes have potency against multiple cancers in clinic or in clinical trials.[5−10] Ru complexes are active against various Pt-resistant cancers and exhibit lower side effects and different mechanisms of action compared to Pt drugs.[11−13] The Ru drug NAMI-A showed potency against metastasis but did not succeed in clinical trials[14,15] but NKP-1339/IT-139 and TLD1433 underwent phase I clinical trials against nonsmall cell lung carcinoma[16,17] and nonmuscle invasive bladder cancer, respectively. The successful completion of phase I and entry into phase II clinical trials of the phototherapeutic TLD1433 has further enhanced the role of Ru as a metal of choice for the design of new anticancer agents.[18,19] Besides, the organometallic ruthenium(II) *p*-cymene motif, modifiable through mono- or bidentate ligands, and halide coordination provide complexes with excellent antiproliferative activity.[20−23] The appropriate choice of mono/bidentate ligands along with the labile halide suitably

Received: September 24, 2021
Published: November 15, 2021

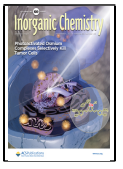

© 2021 American Chemical Society

https://doi.org/10.1021/acs.inorgchem.1c02979
Inorg. Chem. 2021, 60, 18379−18394

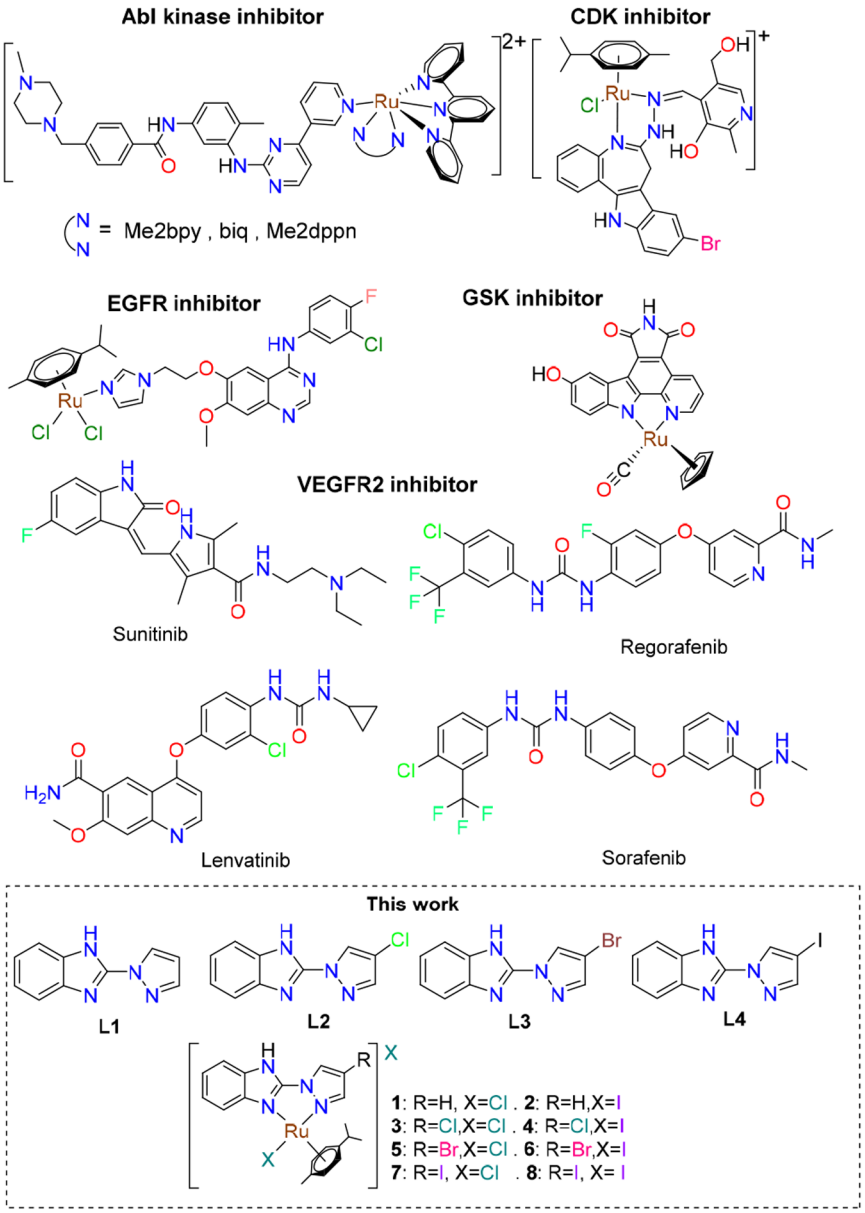

Figure 1. Representative clinically used kinase inhibitors, Ru^{II}-based kinase inhibitors, and the Ru^{II} complexes from this work.

tunes the target selectivity, stability, and pathway of action of ruthenium(II) *p*-cymene complexes because of alteration of the steric and electronic features.[24,25]

Ligand design is a salient aspect to tune the cytotoxicity of metal complexes. In this regard, using organic-directing molecules as ligands to target various cellular events, including impairing protein functions, provides a vital methodology to incorporate multiple pathways of action in a metal complex.[26−29] The "organic-directing molecules" can target various organelles or cellular processes because of their ability to interact with the active site of relevant proteins. Their use as metal-complexing ligands provides the scope of introducing new targets, including cellular proteins and enzymes other than DNA, in the generation of cancer chemotherapeutic agents.[30−34] Organic-directing molecules have been used to target receptor tyrosine kinases (RTKs). Among the RTKs, vascular endothelial growth factor receptor 2 (VEGFR2), a type II transmembrane RTK overexpressed in many tumors, is the principal mediator of vascular endothelial growth factor (VEGF)-induced angiogenic signaling through phosphorylation of the tyrosine(s) in the intracellular domain of VEGFR2. The phosphorylation of VEGFR2 sprouts blood vessel growth (angiogenesis) to ensure an uninterrupted supply of oxygen and nutrients to the fast-proliferating cells.[35−38] Therefore, targeting VEGFR2 receptors is of importance in anticancer drug design.[39−42] Many organic small molecules (Figure 1), including Sunitinib,[43] Sorafenib,[44,45] Regorafenib[46] and Lenvatinib,[47] are reported to inhibit VEGFR2 by interfering with the ATP binding pocket and preventing phosphorylation.[48−54]

Kinases like epidermal growth factor receptor (EGFR) or VEGFR2 are overexpressed in various difficult-to-cure tumors, including triple-negative breast cancers (TNBCs).[55] TNBCs are negative for estrogen, progesterone, and human epidermal growth factor receptor 2 (HER2) receptors.[55] Thus, the growth of the tumor is not fuelled by hormones like estrogen

https://doi.org/10.1021/acs.inorgchem.1c02979
Inorg. Chem. 2021, 60, 18379−18394

or progesterone. So, TNBCs do not respond to hormonal therapy or medicines targeting the HER2 receptors. The treatment primarily relies on small-molecule chemotherapy, including Pt drugs, polyadenosine diphosphate−ribose polymerase inhibitors, microtubule disruptors, immune system adjuvants, and kinase inhibitors.[56−59] The expression of EGFR and VEGFR2 on the cell surface of various TNBCs promotes tumor invasion and metastasis.[55] Thus, inhibition of these proteins and their downstream signaling by small-molecule tyrosine kinase inhibitors is a viable methodology for treatment. During the past 2 decades, various metal complexes (Figure 1) bearing organic-directing groups showed the efficient inhibition of a wide variety of kinases, viz., EGFR, cyclin-dependent kinase (CDK), glycogen synthase kinase 3 beta (GSK 3β), proto-oncogene serine/threonine protein kinase (Pim1), mitogen- and stress-activated protein kinase (MSK1), P21 (RAC1) activated kinase 1 (PAK1), macrophage stimulating 1 (MST1), and myosin light chain kinase (MLCK).[34,60−65] However, metal complexes that efficiently inhibit VEGFR2 phosphorylation are scarce.[66,67] The design of kinase targeting metal complexes benefits from a ligand that alone can target the ATP binding domain in the kinases, and such metal complexes involve the use of derivatives of clinically relevant motifs.[31,66,68] Benzimidazolyl and pyrazolyl compounds are known to be part of a wide variety of clinical drugs with excellent potency, encompassing nonsteroidal antiinflammatory drugs, alkylating agents, anthelmintics, and proton pump inhibitors.[69−75] In this work, we present halido-substituted 2-(1*H*-pyrazol-1-yl)-1*H*-benzo[*d*]imidazole bidentate ligands to design Ru^{II} complexes that inhibit VEGFR2 phosphorylation. We have synthesized and characterized four ligands (**L1**−**L4**), providing eight Ru^{II} complexes (**1**−**8**) with variation of a halide on the 4 position of the pyrazole in the bidentate ligand and in coordination to Ru^{II} (Figure 1). The eight Ru^{II} complexes bear the general molecular formula $[Ru^{II}(p\text{-cym})(L)X]X$, where X = Cl and I. The complexes were characterized by various analytical methods like UV−vis, Fourier transform infrared (FT-IR), ^{1}H, ^{13}C, and HMQC NMR, and high-resolution electrospray ionization mass spectrometry (ESI-HRMS). Complexes **1** and **3** were also characterized by single-crystal X-ray diffraction. The solution stability, cytotoxicity, and VEGFR2 inhibition studies of the corresponding ruthenium(II) *p*-cymene complexes show that the pyrazolylbenzimidazole ligand systems can act as organic-directing groups to inhibit VEGFR2 phosphorylation, while Ru^{II} is capable of DNA binding, thus improving the cytotoxic efficiency.

EXPERIMENTAL SECTION

Materials and Methods. The chemicals were purchased from multiple commercial sources and used without further purification. The solvents were distilled and dried using standard procedures before use.[76] The metal precursor complexes $[Ru^{II}_2(\eta^6\text{-}p\text{-cym})_2(X)_4]$ were synthesized following literature procedures.[77] The solvents used in the spectroscopic measurements were of spectroscopy grade and were purchased from Merck, India. PerkinElmer Lambda 35 and SPECTRUM RX I spectrophotometers were used for UV−vis and FT-IR measurements (in KBr pellets), respectively. The ^{1}H, ^{13}C, and HMQC NMR spectra were recorded using either a 400 MHz JEOL ECS or a 500 MHz Bruker Avance III spectrometer, at room temperature (24−27 °C). The chemical shifts of the relevant compounds are reported in parts per million (ppm). All ESI-HRMS spectra were recorded in electrospray ionization positive mode using a Bruker maXis II TM instrument. Isolated yields of ^{1}H NMR pure compounds are reported. The ligands and complexes synthesized were dried in vacuo and stored in a desiccator in the dark. 3-(4,5-Dimethylthiazol-2-yl)-2,5-diphenyltetrazolium bromide (MTT; USB) and all kind of supplements were purchased from Gibco and used as received for cell culture.

Synthesis and Characterization. *Synthesis of Ligands. Synthesis of Ligands **L1** and **L2**.* The synthesis of respective substituted pyrazoles is provided in the Supporting Information. 1,2-Diaminobenzene (1 mmol) was dissolved in 1 mL of $POCl_3$ (10 mmol). Then the respective pyrazole (1 mmol) was added portionwise. After 10 min of stirring, 0.33 mmol of triphosgene was added over 20 min. The reaction mixture was refluxed for a further 16 h at 110 °C. Then, the reaction was quenched in ice under hot conditions and neutralized with a NaOH solution. At pH 7, a white precipitate appeared. The precipitate was collected by vacuum filtration, and thin-layer chromatography was performed to confirm the purity. A short column over 60−120 mesh silica gel usinga petroleum ether and ethyl acetate mixture (20% for **L1** and a 10−40% gradual increase for **L2**) provided the pure ligands.

*Characterization. 2-(1H-Pyrazol-1-yl)-1H-benzo[d]imidazole (**L1**).* Yield: 98%. ^{1}H NMR (500 MHz, DMSO-d_6, 298 K): δ 13.08 (s, 1H, BzIm-NH), 8.59 (d, J = 2.2 Hz, 1H, pyz-H), 7.95 (s, 1H, pyz-H), 7.58 (s, 1H, BzIm-H), 7.46 (s, 1H, BzIm-H), 7.20 (dd, J = 2.9 Hz, 2H, BzIm-H), 6.66 (s, 1H, pyz-H) (Figure S1). ^{13}C NMR (125 MHz, DMSO-d_6, 298 K): δ 146.0, 142.7, 141.7, 133.6, 128.9, 122.2, 118.3, 111.5, 108.9 (Figure S2). ESI-HRMS (MeOH) for $[HL1]^+ \equiv [C_{10}H_9N_4]^+$: m/z 185.0821 (calcd m/z 185.0822).

*2-(4-Chloro-1H-pyrazol-1-yl)-1H-benzo[d]imidazole (**L2**).* Yield: 83%. ^{1}H NMR (500 MHz, $CDCl_3$, 298 K): δ 8.50 (s, 1H, Pyz-H), 7.69 (s, 1H, Pyz-H), 7.57 (s, 2H, BzIm-H), 7.30 (dd, J = 3.1 Hz, 2H, BzIm-H) (Figure S3). ^{13}C NMR (125 MHz, DMSO-d_6, 298 K): δ 145.3, 141.3, 141.1−140.9, 133.6, 126.9, 122.4, 118.4, 112.5, 111.6 (Figure S4). ESI-HRMS (MeOH) for $[L2 + Na]^+ \equiv [C_{10}H_7ClN_4Na]^+$: m/z 241.0259 (calcd m/z 241.0251).

*Synthesis of Ligands **L3** and **L4**.* The synthesis of respective substituted pyrazoles is provided in the Supporting Information. 1,2-Diaminobenzene (1.0 mmol) was dissolved in 5 mL of dry tetrahydrofuran (THF) at −5 °C under a N_2 atmosphere and stirred for 5 min. Carbonyldiimidazole (CDI; 1.2 mmol) in 5 mL of dry dichloromethane (DCM) was added dropwise over 10 min. The off-white solution turned turbid upon addition, and over time, a white powder precipitated. The precipitate was collected by vacuum filtration after stirring overnight. The precipitate was used for further synthetic steps without any purification. The off-white precipitate of 1,3-dihydro-2*H*-benzo[*d*]imidazol-2-one (1 mmol) and the respective substituted pyrazoles (4-pzBr and 4-pzI; 1.2 mmol) was taken into a tube, and 10 equiv of distilled $POCl_3$ was added slowly. The tube was sealed, heated to 110 °C, and kept at that temperature for 24 h. The resultant hot solution was poured over crushed ice, followed by neutralization with a saturated NaOH solution to bring the pH to ca. 7−8. The solid precipitated was filtered, dried, and separated by column chromatography with petroleum ether/ethyl acetate as the eluent. In the case of **L3**, the initial percentage of ethyl acetate was 5%, which was gradually increased to 20% to complete the elution. To purify **L4**, the initial percentage of ethyl acetate was 5%, which was gradually increased to 15% to complete the elution.

*2-(4-Bromo-1H-pyrazol-1-yl)-1H-benzo[d]imidazole (**L3**).* Yield: 68%. ^{1}H NMR (500 MHz, $CDCl_3$, 298 K): δ 8.54 (d, J = 2.8 Hz, 1H, pyz-H), 7.71 (d, J = 2.7 Hz, 1H, pyz-H), 7.56 (s, 2H, BzIm-H), 7.29 (dt, J = 3.3 Hz, 2H, BzIm-H) (Figure S5). ^{13}C NMR (125 MHz, DMSO-d_6, 298 K): δ 145.7, 143.5, 129.5, 122.8, 118.6, 112.8, 96.9 (Figure S6). ESI-HRMS (MeOH) for $[L3 + Na]^+ \equiv [C_{10}H_7BrN_4Na]^+$: m/z 284.9750 (calcd m/z 284.9746).

*2-(4-Iodo-1H-pyrazol-1-yl)-1H-benzo[d]imidazole (**L4**).* Yield: 63%. ^{1}H NMR (500 MHz, $CDCl_3$, 298 K): δ 8.57 (s, 1H, pyz-H), 7.75 (s, 1H, pyz-H), 7.58 (s, 2H, BzIm-H), 7.29 (dd, J = 3.1 Hz, 2H, BzIm-H) (Figure S7). ^{13}C NMR (125 MHz, DMSO-d_6, 298 K): δ 150.3, 146.6, 141.6, 132.8, 122.9−122.7, 121.8, 118.2, 111.2, 109.2 (Figure S8). ESI-HRMS (MeOH) for $[L4 + Na]^+ \equiv [C_{10}H_7IN_4Na]^+$: m/z 332.9620 (calcd m/z 332.9608).

https://doi.org/10.1021/acs.inorgchem.1c02979
Inorg. Chem. 2021, 60, 18379−18394

Synthesis of Metal Complexes 1−8. General Procedure of the Syntheses of Complexes 1−8. The ligands **L1**−**L4** (0.098 mmol) were added in 15 mL of dry DCM under an inert atmosphere, leading to a suspension. The metal precursor $[Ru^{II}_2(p\text{-cymene})_2Cl_4]$ (0.049 mmol; for **1**, **3**, **5**, and **7**) or $[Ru^{II}_2(p\text{-cymene})_2I_4]$ (0.049 mmol; for **2**,**4**,**6**, and **8**) in 10 mL of dry DCM was added dropwise under a N_2 atmosphere to the above suspension. The solution slowly became transparent. By the time the addition was complete, the color had changed from orange to yellow (for **1**, **3**, **5**, and **7**) or dark red to orange-red (for **2**, **4**, **6**, and **8**). Then turbidity appeared, followed by precipitation. The reaction was left for 24 h to complete and washed five times with diethyl ether (10 mL each) to get rid of excess ligand. The product was collected by vacuum filtration and dried under high vacuum. The purity was confirmed by ^{1}H and ^{13}C NMR, ESI-HRMS, and elemental analysis.

*[Ru^{II}(p-cym)(**L1**)Cl]Cl* (***1***). Yield: 88%. ^{1}H NMR (500 MHz, DMSO-d_6, 298 K): δ 8.96 (d, J = 1.7 Hz, 1H, pyz-H), 8.88 (d, J = 2.9 Hz, 1H, pyz-H), 7.99 (d, J = 7.8 Hz, 1H, BzIm-H), 7.69 (d, J = 7.8 Hz, 1H, BzIm-H), 7.48−7.40 (m, 2H, BzIm-H), 7.06−7.03 (m, 1H, pyz-H), 6.33 (dd, J = 9.6 and 6.2 Hz, 2H, *p*-cym-H), 6.18 (d, J = 6.0 Hz, 1H, *p*-cym-H), 6.10 (d, J = 6.0 Hz, 1H, *p*-cym-H), 2.59 (dd, J = 13.7 Hz, 1H*p*-cym-isopropyl-CH), 2.15 (s, 3H, *p*-cym-Me), 1.03 (d, J = 6.9 Hz, 3H,*p*-cym-isopropyl), 0.98 (d, J = 6.9 Hz, 3H, *p*-cym-isopropyl). ^{13}C NMR (125 MHz, DMSO-d_6, 298 K): δ 148.1, 144.9, 139.1, 130.9, 124.2, 123.8, 116.7, 113.8, 112.1, 103.4, 101.6, 83.6, 82.3, 81.4, 80.3, 30.5, 21.8, 21.7, 18.4 (Figures S9−S11). IR (KBr pellets, cm^{-1}): 3419, 1767, 1595, 1351, 749. UV−vis [MeOH; λ_{max}, nm (ε, M^{-1} cm^{-1})]: 298 (21016), 417 (606) (Figure S33). ESI-HRMS (MeOH) for $[\mathbf{1} - Cl - HCl]^+ \equiv [C_{20}H_{21}N_4Ru]^+$: m/z 419.0770 (calcd m/z 419.0810). Anal. Calcd for $C_{20}H_{22}Cl_2N_4Ru$: C, 48.99; H, 4.52; N, 11.43. Found: C, 49.19; H, 4.60; N, 11.83.

*[Ru^{II}(p-cym)(**L1**)I]I* (***2***). Yield: 82%. ^{1}H NMR (500 MHz, DMSO-d_6, 298 K): δ 8.92 (d, J = 1.9 Hz, 1H, pyz-H), 8.70 (d, J = 3.0 Hz, 1H, pyz-H), 7.90 (d, J = 7.1 Hz, 1H, BzIm-H), 7.73 (d, J = 7.1 Hz, 1H, BzIm-H), 7.49−7.39 (m, 2H, BzIm-H), 7.08−7.02 (m, 1H, pyz-H), 6.27 (d, J = 6.4 Hz, 2H, *p*-cym-H), 6.14 (dd, J = 5.0 Hz, 2H, *p*-cym-H), 2.76 (dt, J = 13.8 Hz, 1H, *p*-cym-isopropyl-CH), 2.34 (s, 3H, *p*-cym-Me), 1.05 (dd, J = 6.9 Hz, 6H, *p*-cym-isopropyl). ^{13}C NMR (125 MHz, DMSO-d_6, 298 K): δ 149.6, 140.2, 130.9, 124.2, 123.9, 117.1, 114.5, 112.7, 106.1, 100.7, 83.4, 82.5, 82.2, 31.6, 22.4, 21.9, 20.3 (Figures S12−S14). IR (KBr pellets, cm^{-1}): 3420, 1767, 1594, 1355, 776. UV−vis [MeOH; λ_{max}, nm (ε, M^{-1} cm^{-1})]: 296 (27823), 444 (882) (Figure S33). ESI-HRMS (MeOH) for $[\mathbf{2} - I]^+ \equiv [C_{20}H_{22}IN_4Ru]^+$: m/z 546.9952 (calcd m/z 546.9933). Anal. Calcd for $C_{20}H_{22}I_2N_4Ru$: C, 35.68; H, 3.29; N, 8.32. Found: C, 35.39; H, 3.14; N, 8.24.

*[Ru^{II}(p-cym)(**L2**)Cl]Cl* (***3***). Yield: 90%. ^{1}H NMR (500 MHz, DMSO-d_6, 298 K): δ 9.34 (s, 1H, pyz-H), 9.29 (s, 1H, pyz-H), 8.01 (d, J = 7.8 Hz, 1H, BzIm-H), 7.69 (d, J = 7.7 Hz, 1H, BzIm-H), 7.45 (dd, J = 7.8 Hz, 2H, BzIm-H), 6.37 (d, J = 6.0 Hz, 1H, *p*-cym-H), 6.34 (d, J = 6.1 Hz, 1H, *p*-cym-H), 6.16 (dd, J = 6.1 Hz, 2H, *p*-cym-H), 2.65 (dt, J = 13.8 Hz, 1H, *p*-cym-isopropyl-CH), 2.14 (s, 3H, *p*-cym-Me), 1.06 (d, J = 6.9 Hz, 3H, *p*-cym-isopropyl), 1.02 (d, J = 6.9 Hz, 3H, *p*-cym-isopropyl). ^{13}C NMR (125 MHz, DMSO-d_6): δ 145.8, 144.9, 139.2, 128.8, 124.2, 123.8, 116.7, 114.2, 113.9, 103.9, 101.4, 83.2, 82.2, 81.6, 80.7, 30.5, 21.8, 18.4 (Figures S15−S17). IR (KBr pellets, cm^{-1}) 3414, 1747, 1595, 1367, 804. UV−vis [MeOH; λ_{max}, nm (ε, M^{-1} cm^{-1})]: 304 (11978), 415 (523) (Figure S33). ESI-HRMS (MeOH) for $[\mathbf{3} - Cl - HCl]^+ \equiv [C_{20}H_{20}ClN_4Ru]^+$: m/z 453.0416 (calcd m/z 453.0420). Anal. Calcd for $C_{20}H_{21}Cl_3N_4Ru$: C, 45.77; H, 4.03; N, 10.68. Found: C, 45.64; H, 3.94; N, 10.71.

*[Ru^{II}(p-cym)(**L2**)I]I* (***4***). Yield: 85%. ^{1}H NMR (500 MHz, DMSO-d_6, 298 K): δ 9.17 (s, 1H, pyz-H), 8.92 (s, 1H, pyz-H), 7.88 (d, J = 7.8 Hz, 1H, BzIm-H), 7.70 (d, J = 7.5 Hz, 1H, BzIm-H), 7.40 (dd, J = 7.9 Hz, 2H, BzIm), 6.29 (d, J = 6.0 Hz, 1H, *p*-cym-H), 6.23 (d, J = 6.1 Hz, 1H, *p*-cym-H), 6.16 (d, J = 6.1 Hz, 1H, *p*-cym-H), 6.12 (d, J = 6.0 Hz, 1H, *p*-cym-H), 2.78 (dt, J = 13.6 Hz, 1H, *p*-cym-isopropyl-CH), 2.34 (s, 3H, *p*-cym-Me), 1.06 (t, J = 7.1 Hz, 6H, *p*-cym-isopropyl). ^{13}C NMR (125 MHz, DMSO-d_6, 298 K): δ 146.9, 144.3, 140.1, 128.6, 124.1, 123.8, 116.7, 114.6, 114.1, 106.3, 100.4, 82.9, 82.3, 81.8, 31.3, 22.0, 21.8, 19.9 (Figures S18−S20). IR (KBr pellets, cm^{-1}): 3421, 1773, 1524, 1329, 839. UV−vis [MeOH; λ_{max}, nm (ε, M^{-1} cm^{-1})]: 305 (17952), 444 (947) (Figure S33). ESI-HRMS (MeOH) for $[\mathbf{4} - I - HI]^+ \equiv [C_{20}H_{20}ClN_4Ru]^+$: m/z 453.0481 (calcd m/z 453.0420). Anal. Calcd for $C_{20}H_{21}ClI_2N_4Ru$: C, 33.94; H, 2.99; N, 7.92. Found: C, 34.10; H, 2.77; N, 8.03.

*[Ru^{II}(p-cym)(**L3**)Cl]Cl* (***5***). Yield: 92%. ^{1}H NMR (500 MHz, DMSO-d_6, 298 K): δ 9.19 (s, 1H, pyz-H), 9.08 (s, 1H, pyz-H), 7.96 (d, J = 7.9 Hz, 1H, BzIm-H), 7.68 (d, J = 7.8 Hz, 1H, BzIm-H), 7.41 (dt, J = 7.3 Hz, 2H, BzIm-H), 6.35 (d, J = 6.0 Hz, 1H, *p*-cym-H), 6.31 (d, J = 6.1 Hz, 1H, *p*-cym-H), 6.13 (dd, J = 6.1 Hz, 2H, *p*-cym-H), 2.62 (dt, J = 13.7 Hz, 1H,*p*-cym-isopropyl-CH), 2.14 (s, 3H *p*-cym-Me), 1.02 (dd, J = 6.9 Hz, 6H, *p*-cym-isopropyl). ^{13}C NMR (125 MHz, DMSO-d_6, 298 K): δ 147.6, 144.7, 139.2, 130.9, 124.2, 123.9, 116.7, 114.1, 104.1, 101.4, 98.1, 83.2, 82.2, 81.6, 80.7, 30.6, 21.8, 18.4 (Figures S21−S23). IR (KBr Pellets, cm^{-1}): 3422, 1691, 1591, 1400, 808. UV−vis [MeOH; λ_{max}, nm (ε, M^{-1} cm^{-1})]: 304 (15563), 417 (603) (Figure S33). ESI-HRMS (MeOH) for $[\mathbf{5} - Cl - HCl]^+ \equiv [C_{20}H_{20}BrN_4Ru]^+$: m/z 496.9896 (calcd m/z 496.9915). Anal. Calcd for $C_{20}H_{21}BrCl_2N_4Ru$: C, 42.20; H, 3.72; N, 9.84. Found: C, 41.99; H, 3.64; N, 9.81

*[Ru^{II}(p-cym)(**L3**)I]I* (***6***). Yield: 84%. ^{1}H NMR (500 MHz, DMSO-d_6, 298 K): δ 9.15 (s, 1H, pyz-H), 8.90 (s, 1H, pyz-H), 7.88 (d, J = 7.8 Hz, 1H, BzIm-H), 7.70 (d, J = 7.5 Hz, 1H, BzIm-H), 7.41 (t, J = 8.0 Hz, 2H, BzIm-H), 6.29 (d, J = 6.0 Hz, 1H, *p*-cym-H), 6.23 (d, J = 6.1 Hz, 1H, *p*-cym-H), 6.16 (d, J = 6.0 Hz, 1H, *p*-cym-H), 6.11 (d, J = 6.0 Hz, 1H, *p*-cym-H), 2.77 (dd, J = 13.7 Hz, 1H,*p*-cym-isopropyl-CH), 2.33 (s, 3H, *p*-cym-Me), 1.05 (t, J = 6.6 Hz, 6H, *p*-cym-isopropyl). ^{13}C NMR (125 MHz, DMSO-d_6, 298 K): δ 148.7, 144.2, 130.6, 124.13, 116.7, 114.6, 106.3, 100.4, 98.1, 83.0, 82.3, 81.8, 31.3, 22.00, 21.8, 19.9 (Figures S24−S26). IR (KBr pellets, cm^{-1}): 3418, 1773, 1582, 1389, 842. UV−vis [MeOH; λ_{max}, nm (ε, M^{-1} cm^{-1})]: 307 (16840), 447 (979) (Figure S33). ESI-HRMS (MeOH) for $[\mathbf{6} - I]^+ \equiv [C_{20}H_{21}BrIN_4Ru]^+$: m/z 624.8998 (calcd m/z 624.9038). Anal. Calcd for $C_{20}H_{21}BrI_2N_4Ru$: C, 31.94; H, 2.81; N, 7.45. Found: C, 31.72; H, 2.71; N, 7.27.

*[Ru^{II}(p-cym)(**L4**)Cl]Cl* (***7***). Yield: 85%. ^{1}H NMR (500 MHz, DMSO-d_6, 298 K): δ 9.12 (s, 1H, pyz-H), 8.98 (s, 1H, pyz-H), 7.97 (d, J = 7.8 Hz, 1H, BzIm-H), 7.68 (d, J = 7.7 Hz, 1H, BzIm-H), 7.42 (dt, J = 7.2 Hz, 2H, BzIm-H), 6.35 (d, J = 5.9 Hz, 1H, *p*-cym-H), 6.30 (d, J = 6.0 Hz, 1H, *p*-cym-H), 6.13 (t, J = 7.0 Hz, 2H, *p*-cym-H), 2.63−2.58 (m, 1H, *p*-cym-isopropyl-CH), 2.13 (s, 3H, *p*-cym-Me), 1.02 (dd, J = 6.8 Hz, 6H, *p*-cym-isopropyl). ^{13}C NMR (125 MHz, DMSO-d_6, 298 K): δ 151.7, 144.1, 138.99, 134.9, 124.4, 123.9, 116.8, 113.9, 103.9, 101.4, 83.3, 82.2, 81.6, 80.8, 30.6, 21.8, 18.4 (Figures S27−S29). IR (KBr pellets, cm^{-1}): 3428, 1592, 1455, 1059, 856. UV−vis [MeOH; λ_{max}, nm (ε, M^{-1} cm^{-1})]: 305 (14713), 420 (531) (Figure S33). ESI-HRMS (MeOH) for $[\mathbf{7} - Cl - HCl]^+ \equiv [C_{20}H_{20}IN_4Ru]^+$: m/z 544.9723 (calcd m/z 544.9776). Anal. Calcd for $C_{20}H_{21}Cl_2IN_4Ru$: C, 38.98; H, 3.43; N, 9.09. Found: C, 39.31; H, 3.54; N, 8.74.

*[Ru^{II}(p-cym)(**L4**)I]I* (***8***). Yield: 87%. ^{1}H NMR (500 MHz, DMSO-d_6, 298 K): δ 9.09 (s, 1H, pyz-H), 8.81 (s, 1H, pyz-H), 7.89 (d, J = 7.7 Hz, 1H, BzIm-H), 7.71 (d, J = 7.4 Hz, 1H, BzIm-H), 7.43 (t, J = 7.3 Hz, 2H, BzIm-H), 6.30 (d, J = 6.0 Hz, 1H, *p*-cym-H), 6.23 (d, J = 6.0 Hz, 1H, *p*-cym-H), 6.16 (d, J = 6.1 Hz, 1H, *p*-cym-H), 6.11 (d, J = 6.0 Hz, 1H, *p*-cym-H), 2.80−2.74 (m, 1H, *p*-cym-isopropyl-CH), 2.32 (s, 3H, *p*-cym-Me), 1.05 (t, J = 6.4 Hz, 6H, *p*-cym-isopropyl). ^{13}C NMR (125 MHz, DMSO-d_6): δ 149.3, 144.5, 140.5, 131.0, 124.4, 124.1, 123.6, 117.3, 114.3, 106.8, 101.1, 98.0, 83.4, 82.3, 81.3, 31.3, 22.3, 21.8, 19.9 (Figures S30−S32). IR (KBr pellets, cm^{-1}): 3425, 1955, 1591, 1152, 695. UV−vis [MeOH; λ_{max}, nm (ε, M^{-1} cm^{-1})]: 308 (17933), 446 (1039) (Figure S33). ESI-HRMS (MeOH) for $[\mathbf{8} - I]^+ \equiv [C_{20}H_{21}I_2N_4Ru]^+$: m/z 672.8870 (calcd m/z 672.8899). Anal. Calcd for $C_{20}H_{21}I_3N_4Ru$: C, 30.06; H, 2.65; N, 7.01. Found: C, 30.21; H, 2.71; N, 6.93.

X-ray Crystallography. The attempts to crystallize the complexes provided us with good-diffraction-quality single crystals of complexes **1** and **3**. The crystals were obtained by layering diethyl ether over a methanol (MeOH) solution of **1** or **3** and keeping them in a

https://doi.org/10.1021/acs.inorgchem.1c02979
Inorg. Chem. 2021, 60, 18379−18394

refrigerator in sealed condition for 2 weeks. Suitable yellow-orange transparent single crystals were mounted over a goniometer loop of a SuperNova, Dual, Cu at zero, Eos diffractometer. The data collection temperature was 293(2) K for **1** and 100(10) K for **3** with Cu Kα as the X-ray source (λ = 1.5406 Å). Data reduction was performed with *CrysAlisPro 171.37.33c* (Agilent Technologies). Finally, the structures were solved using the *ShelXT* structure solution program[78] with intrinsic phasing and refined with the *ShelXL*[78] refinement package using least-squares minimization in *Olex2*.[79] An anisotropic displacement parameter was used for all of the non-hydrogen atoms. All of the hydrogen atoms were calculated and fixed after hybridization of the non-hydrogen atoms (Figures 2 and S34). A few important structural pieces of information and crystallographic parameters are listed in Tables 1 and S1, respectively. The deposition numbers for the crystal structures are CCDC 2087583 (**1**) and 2087584 (**3**). The residual electron density of 2.6 Å^3 at a distance of 0.9 Å from Ru1 for complex **3** is due to the relatively poor quality of the crystal.

Solution Stability. A stability study of complexes **3**, **5**, **7**, and **8** was performed using ^{1}H NMR in dimethyl sulfoxide (DMSO)-d_6 and a 10 mM phosphate buffer at pH* 7.4 [pH meter reading without correction for the effects of deuterium on the glass electrode; 3:7 (v/v)] containing 4 mM NaCl at 37 °C at various time intervals for 72 h (Figures 3 and S35−S38). The halide exchange studies of the iodido complexes **4**, **6**, and **8** were performed at 27 °C for 24 h similarly except that the NaCl concentration was 130 mM (Figures S39−S41).

Determination of the Distribution Coefficient. The distribution coefficient (log $D_{o/w}$) was determined by following the OECD guidelines[80] using the shake-flask method. A known amount of the respective complex (**1**−**8**) is solubilized in *n*-octanol (presaturated with deionized water) and continuously shaken for 6 h on an orbital shaker at 37 °C. Upon completion, the biphasic solutions were centrifuged for 3 min to allow complete phase separation. Then aliquots from each layer were measured separately upon adequate dilution (ca. 10 times diluted) in a UV−vis spectrophotometer using proper dilution to obtain the absorbance below 1 for absorption maxima of ca. 298−308 nm. The concentration of the complexes remaining in the *n*-octanol phase was determined and subtracted from the originally dissolved concentration, which gave the concentration of the complexes in the water phase. The distribution coefficients (log $D_{o/w}$) of the complexes were obtained from the concentration ratio of the complexes present in the *n*-octanol and water phase (Figure 4A).

Cellular Accumulation of Ru by Inductively Coupled Plasma Optical Emission Spectrometry (ICP-OES). Around 5 × 10^5 of the metastatic triple-negative breast carcinoma (MDA-MB-231) cells were seeded in a 100 mm sterile tissue culture Petri dish and grown for 48 h, leading to 80% confluency of the cells. To these cells in the respective wells, 10 μM metal complexes (**1**−**8**) were added and incubated for another 12 h. After 12 h, the medium was discarded, and the cells were thoroughly washed with 1X phosphate-buffered saline (PBS; pH 7.2). The drug-treated cells were then harvested by trypsinization, and each set of duplicates was counted accurately, followed by centrifugation to obtain cell pellets. The cell pellets were washed twice by 1X PBS (pH 7.2). Finally, the cells were digested with 200 μL of extra pure [70% (v/v)] nitric acid (Sigma-Aldrich) at 70 °C for 12 h. The digested cell suspension was then diluted to 10 mL using Milli-Q water, and the Ru content in the samples was analyzed on a Thermo Scientific iCAP 7400 ICP-OES instrument. Ru standard solutions were freshly prepared before the experiments to generate the best calibration curve in *GraphPad Prism*, version 5.03 (Figure 4B).

Interaction with the Model Nucleobase 9-Ethylguanine (9-EtG). Complexes **3** and **7** were studied with 9-EtG using ^{1}H NMR in DMSO-d_6/10 mM phosphate buffer [3:7 (v/v)] at pH* 7.4 containing 4 mM NaCl at 37 °C at various time intervals for a 72 h period. The binding to 9-EtG was confirmed by the downfield chemical shift of H8 of 9-EtG along with analysis of the other required peaks (Figures 6C and S42 and S43). The 9-EtG-bound species were identified by ESI-MS using 1:9 (v/v) MeOH/10 mM phosphate buffer of pH 7.4 and 4 mM NaCl (Figures 6A,B and S54−S57).

Cell Line and Culture Condition. The MDA-MB-231 cells were obtained from NCCS, Pune, India. The cells were grown as an adherent monolayer in a 100 mm Petri dish in a 5% CO_2 atmosphere using 1:1 mixture of Dulbecco's modified Eagle medium (DMEM) and Ham's F12 nutrient mixture as a culture medium, supplemented with 10% fetal bovine serum (FBS; Gibco) and antibiotics (100 unit mL^{-1} penicillin and 100 μg mL^{-1} streptomycin). The cell line was maintained at its logarithmic growth phase before every experiment and seeded when it became 70% confluent.

Cell Viability Assay. The inhibitory effect of complexes **1**−**8** on the growth of the MDA-MB-231 cell line was assessed with the help of MTT assay. In brief, 6 × 10^3 cells well^{-1} were seeded in 96-well microplates in a DMEM/F12 culture medium (200 μL) and incubated at 37 °C in a 5% CO_2 atmosphere. After 24 h of incubation, the existing medium was replaced by a fresh medium (200 μL). The complexes **1**−**8** to be tested were dissolved in a minimum volume of DMSO (for cisplatin, we used *N*,*N*-dimethylformamide),[81] and an appropriate concentration was added in triplicate to the respective wells such that the concentration of DMSO does not exceed 0.2% in each well. After 72 h of incubation with the drug, the drug-containing medium was replaced with a fresh one, followed by the addition of 20 μL of a 1 mg mL^{-1} MTT solution in 1X PBS (pH 7.2). After incubation with MTT for 3 h at 37 °C, the medium was removed, and the purple crystals of formazan were dissolved in 200 μL of DMSO. The inhibition of the cell growth was evaluated by measuring the absorbance of the drug-treated wells with respect to the untreated controls at 570 nm using a Biotek H1M multimode plate reader. The IC_{50} values (drug concentrations responsible for 50% growth inhibition of the cells) were calculated by fitting nonlinear four-parameter curves using a dose-response inhibition−variable slope model through *GraphPad Prism 5*, version 5.03 (Figure S58). The data represented in Table 2 are the mean of three independent experiments, where each concentration was repeated in triplicate.

VEGFR2 Inhibition: Western Blot and Immunoprecipitation (IP). To determine the effect of the ligands and corresponding complexes on VEGFR2 signaling in the MDA-MB-231 cell line, we investigated Y_{1175} phosphorylation of VGEFR2 and the total tyrosine phosphorylation of Src and ERK1/2.[82,83] MDA-MB-231 cells were grown in DMEM/F12 (1:1), supplemented with 10% heat-inactivated FBS and antibiotics at 37 °C in 5% CO_2. The cells were grown to 80% confluency and then treated with DMSO (0.2%) vehicle control or 5 and 10 μM **L2**, **L4**, **3**, and **7**. After incubation, the cells were activated by 60 nM $VEGF_{165a}$ for 5 min. The activated cells were harvested and lysed with a radio-immunoprecipitation assay lysis buffer [25 mM Tris-HCl (pH 7.5), 1 mM ethylenediaminetetraacetic acid (EDTA), 100 mM NaCl, 1% Nonidet P40, and 1% Triton X-100], supplemented with 0.1 mM vanadate and a protease inhibitor cocktail (5 mg L^{-1} leupeptin, 0.1 mM phenylmethylsulfonyl fluoride, and 2 mM benzamidine). The cell lysate was sonicated and cleared by centrifuging at 500*g* for 10 min. One fraction of the supernatant was used for VEGFR2 immunoblot; another fraction was incubated with 5 μg of Src antibody and 3.5 μg of ERK1/2 antibody overnight at 4 °C IP. After overnight incubation, it was further incubated with 30 μL of protein G beads for 2 h. The beads were washed four times with ice-cold PBS, supplemented with 2 mM sodium orthovanadate. The samples were boiled with a Laemmle sample buffer and run in sodium dodecyl sulfate−polyacrylamide gel electrophoresis (SDS-PAGE). Following SDS-PAGE, lysates were transferred onto nitrocellulose paper and blocked with 5% skim milk in Tris-buffered saline with 0.1% Tween 20 (TBST) for 2 h at room temperature. The blocked membrane was incubated overnight at 4 °C with anti Src, ERK1/2, or VEGFR2 antibody for checking the loading and with anti pY_{1175} VEGFR2 or anti pY antibody for checking the phosphorylation level, followed by 2 h of incubation with horseradish peroxidase-conjugated anti-mouse or anti-rabbit secondary antibody (Figures 7 and S59).

Cell Cycle Analysis. The 2 ×10^5 MDA-MB-231 cells were seeded in a 6-well plate in a DMEM/F12 culture medium and incubated at 37 °C in a 5% CO_2 atmosphere. The medium was renewed after 48 h. Then the IC_{20} and IC_{50} concentrations of complexes **3** and **7** were added and incubated for 8 h. After drug exposure, cells were harvested

https://doi.org/10.1021/acs.inorgchem.1c02979
Inorg. Chem. 2021, 60, 18379−18394

quickly by trypsinization and washed twice with cold 1X PBS (pH 7.2). The cells were resuspended in 100 μL of cold 1X PBS and fixed with 70% chilled aqueous ethanol overnight at 4 °C. DNA staining was performed by resuspending the cell pellets in a 1X PBS solution containing a PI (55 μg mL^{-1}) and RNase A (100 μg mL^{-1}) solution. The cell suspension was gently mixed with a PI staining solution and incubated at 37 °C for 30 min. Samples were analyzed in a BD Biosciences FACSCalibur or BD LSRFortessa flow cytometer (Figures 8C,D and S60).

Detection of Apoptosis: Annexin-V-PE/7AAD Assay. A flow cytometric method was used for apoptosis detection using an Annexin V-PE/7-AAD dual-staining detection kit (BD Pharmigen). The manufacturer's protocol was followed. Briefly, 5 × 10^4 cells were seeded in a 35 mm Petri dish with 2 mL of a DMEM/F12 cell culture medium. The cells were incubated for 48 h in a 5% CO_2 environment. After that, the medium was renewed, and the cells were treated with an appropriate concentration of the drug solution (IC_{20} and IC_{50}) of complexes **3** and **7** for 8 h. The cells were harvested with cold 1X PBS containing 0.1 mM EDTA, followed by washing twice with cold 1X PBS. Then the cells were resuspended in a 1X Annexin V binding buffer. The cells were incubated with both Annexin V-PE and 7-AAD in dark conditions for 15 min at 25 °C. Data were collected and analyzed in a BD Biosciences FACS Calibur or a BD LSRFortessa flow cytometer within 1 h of sample preparation (Figures 8A,B and S61).

***In Vivo* Antiangiogenesis on Zebrafish.** *Animal Husbandry and Breeding.* Zebrafish usually start breeding at the onset of light (7 AM). Pairwise breeding was set on a sloping breeding tank filled with water in the evening of the previous day after feeding at 6:30 PM. Four females and two males were kept in the breeding tank to maintain a female/male ratio of 2:1. They frequently bred the next morning when the light appeared at 7 AM. Enough eggs (~500 eggs) were found at the bottom of the tank. These eggs were collected subsequently using a strainer, transferred into the Petri dish (with an average of 25 embryos/Petri dish) by rinsing the strainer with a 1X E3 medium (5 mM NaCl, 0.17 mM KCl, 0.33 mM $CaCl_2$, 0.33 mM $MgSO_4$, and 10−5% methylene blue), and kept in the incubator at 28.4 °C.

Drug Treatment. A transgenic line of zebrafish embryos [Tg-(fli1:gfp)] was incubated overnight with drugs (**L2**, 25 μM; **3**, 50 μM) along with the vehicle control DMSO at the 13 somite stage, approximately 14 h postfertilization (hpf) before intersegmental vessels (ISVs), dorsal aorta, duct of Cuvier, and caudal vein were formed. The embryos were treated with specific doses of the drug and transferred into a fresh 1X E3 medium after 12 h of drug incubation. The embryos were treated in the anesthetic Tricaine (ethyl 3-aminobenzoate) solution (25× stock solution of Tricaine at 4 mg mL^{-1} in 20 mM Tris pH 8.8 and brought down to pH 7, aliquoted by 4 mL, and stored at −20 °C) for a few minutes to make them still, followed by taking multiple confocal images at 30 and 48 hpf using a Nikon confocal microscope, and the corresponding images were processed in NIS-Elements viewer 5.21 software (Figure 9).

RESULTS AND DISCUSSION

Synthesis of the *N*,*N*-chelating ligands **L1**−**L4** used direct and metal-free amination of the cyclic urea with halo-substituted pyrazoles by refluxing in $POCl_3$ for 16 h (Scheme 1). **L1** and **L2** were synthesized by a three-component one-pot approach using *o*-phenylenediamine, triphosgene, and pyrazoles.[84] The cyclic urea, an essential intermediate for **L3** and **L4**, was synthesized from *o*-phenylenediamine and CDI in a dry THF/DCM mixture at low temperature under an inert atmosphere.[85] **L3** and **L4** were synthesized from the cyclic urea and respective pyrazoles using CDI coupling.[86,87] We have employed a one-pot coupling method to prepare four ligands (**L1**−**L4**)[84] as discussed in the Experimental Section. All of the reactions were conducted in a Teflon-cap-sealed glass tube. After completion of the reaction, excess $POCl_3$ was quenched with a saturated NaOH solution to adjust the pH at ca. 7−8 for adequate precipitation. All of the pure ligands (**L1**−**L4**) were isolated in good yields (63−98%) after column chromatography. The chlorido complexes (**1**, **3**, **5**, and **7**) were synthesized from $Ru^{II}_2(p\text{-cym})_2Cl_4$, and the iodido complexes (**2**, **4**, **6**, and **8**) were synthesized from $Ru^{II}_2(p\text{-cym})_2I_4$ by refluxing the respective bidentate ligands **L1**−**L4** in dry DCM with stirring for 24 h under an inert atmosphere. All metal complexes (**1**−**8**) were characterized by ^{1}H, ^{13}C, and HMQC NMR, FT-IR, and UV−vis spectroscopy along with ESI-HRMS. Complexes **1** and **3** were also characterized by single-crystal X-ray crystallography. The bulk purity of the complexes was determined by elemental analysis. The UV−vis spectra of the complexes showed two different bands at 250−330 nm, corresponding to a $\pi-\pi^*$ transition in the ligands, and 400−500 nm, which may correspond to contributions from both charge-transfer and d−d transitions (Figure S33).

X-ray Crystallography. Suitable good-quality single crystals of complexes **1** and **3** were obtained by layering their respective methanolic solution with diethyl ether. Complexes **1** and **3** crystallize as a mixture of enantiomers (racemic mixtures) in the monoclinic crystal system in space groups $P2_1/n$ and $P2_1/c$, respectively (Table S1). The single-crystal structures of **1** and **3** revealed that the Ru^{II} center is coordinated by $N_{pz}-N_{Bz}$ of the bidentate ligands along with *p*-cymene and chloride. The *p*-cymene ring is bound to Ru in a η^6 fashion. In complex **1**, the methyl group of *p*-cymene is directed toward the bidentate ligand, whereas the isopropyl group is used for for complex **3**. Hence, the Ru1−N1 bond length in complex **3** (2.112 Å) is higher than that of complex **1** (2.097 Å; Table 1). The presence of an electronegative chloride atom with a pyrazole ring in complex **3** has no effect on the structure because the Ru1−N3 bond length (2.107 Å) is almost equal to complex **1** (2.108 Å; Table 1). Each unit cell consists of four molecules of **1** and **3** with chloride counteranions (Figure S34) to balance the residual monopositive charge of Ru^{II}. The Ru^{II} center adopts a pseudooctahedral geometry (Figure 2). The Ru−C bond distances in *p*-cymene range from 2.16 to 2.20 Å for both **1** and **3**. The Ru−Cl bond distances in both complexes are ca. 2.40 Å. The bond angles of N_{pz}−Ru−Cl in **1** and **3** (∠N3−Ru1−Cl1) are ca. 85.9° and 85.6°, respectively. The bond angles of $\angle N_{Bz}$−Ru−Cl in both complexes (∠N1−Ru1−Cl1) are ca. 85.4° and

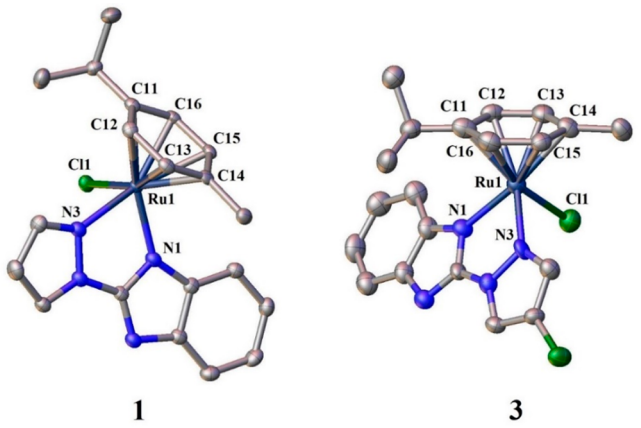

Figure 2. ORTEP diagram of complexes **1** and **3**. Thermal ellipsoids are drawn at 50% probability. All hydrogen atoms and counteranions were omitted for clarity.

https://doi.org/10.1021/acs.inorgchem.1c02979
Inorg. Chem. 2021, 60, 18379−18394

Table 1. Selected Bond Distances (Å) and Angles (deg) for Complexes 1 and 3 as Labeled in Figure 2

1				3			
Ru1−Cl1	2.404(5)	N1−Ru1−N3	76.05(8)	Ru1−Cl1	2.401(2)	N3−Ru1−N1	75.9(2)
Ru1−N1	2.097(2)	N1−Ru1−Cl1	85.43(5)	Ru1−N1	2.112(6)	N1−Ru1−Cl1	86.41(19)
Ru1−N3	2.108(2)	N3−Ru1−Cl1	85.89(5)	Ru1−N3	2.107(7)	N3 Ru1 Cl1	85.67(19)
Ru1−C11	2.202(2)	N1−Ru1−C11	166.83(8)	Ru1−C11	2.197(10)	N1−Ru1−C11	92.10(3)
Ru1−C12	2.173(2)	N1−Ru1−C12	149.91(8)	Ru1−C12	2.188(8)	N1−Ru1−C12	101.2(3)
Ru1−C13	2.163(2)	N1−Ru1−C13	113.49(8)	Ru1−C13	2.185(8)	N1−Ru1−C13	130.8(3)
Ru1−C14	2.193(2)	N1−Ru1−C14	92.54(8)	Ru1−C14	2.219(8)	N1−Ru1−C14	168.4(3)
Ru1−C15	2.194(2)	N1−Ru1−C15	100.00(8)	Ru1−C15	2.181(7)	N1−Ru1−C15	148.2(3)
Ru1−C16	2.177(2)	N1−Ru1−C16	128.60(8)	Ru1−C16	2.182(9)	N1−Ru1−C16	112.2(3)

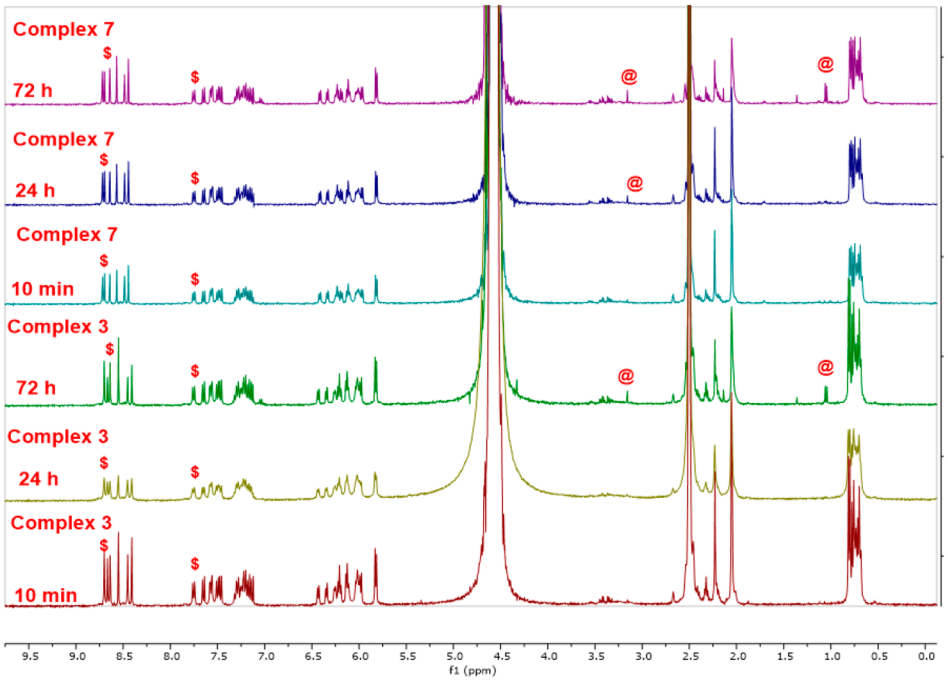

Figure 3. Solution stability of the chlorido complexes 3 and 7 in a 10 mM phosphate buffer (pH* 7.4) with 4 mM NaCl in 30% DMSO-d_6. Aquated species are shown by $, and free *p*-cymene species are shown by @.

86.4°, respectively. The Ru−N and Ru−Cl distances and N−Ru−Cl angles are in good agreement with similar complexes[65,88] and support the deviation from the ideal octahedral geometry. The counteranion chloride is hydrogen-bonded (intramolecular) with N−H of benzimidazole (N−H···Cl), displaying distances of 3.009 and 3.058 Å respectively in **1** and **3** (Figure S34).

Solution Stability. The Ru^{II} complexes were selectively investigated through ^{1}H NMR for aqueous stability by dissolving in a mixture of 3:7 (v/v) DMSO-d_6/10 mM phosphate buffer (pH* 7.4). The chlorido complexes (**3**, **5**, and **7**) were studied in the presence of 4 mM NaCl at 37 °C for 72 h, and they aquated immediately under these conditions. After formation of the aquated complexes, there is very little change, showing that the aquated complexes are the major form (ca. 70%) in solution during the 72 h period (Figures 3 and S35, S36, and S37). There is a small amount of arene loss (free *p*-cymene signals at 2.18, 1.10, and 7.18 ppm)[65] starting from 48 h, which is less than 30% even at 72 h (indicated by @ in Figure 3). It must be noted here that we could not identify any peaks corresponding to an unbound ligand or the dinuclear ruthenium(II) *p*-cymene precursor in solution for any of the complexes. In many cases, the stability constants of N,N-coordinated ruthenium(II) *p*-cymene complexes are reported, and the values endorse their high stability in aqueous solution.[26,89,90] The iodido complex **8** is more than 95% intact and displays no arene loss or formation of the aquated complex like **7** during the 72 h period at 37 °C (Figure S38).The ruthenium(II) *p*-cymene complexes **7** and **8**, of **L4**, are the most soluble ones. In the presence of 130 mM NaCl, the chloride exchange initiated rapidly in the iodido complexes **4**, **6**, and **8** at 27 °C, and after ca. 50% exchange, there is equilibration under the NMR tube conditions and the data show no further change up to the monitored period of 24 h (Figures S39−S41).

The ESI-MS studies also support the NMR data that the chlorido coordination is more labile than the iodido coordination. A 200 μM stock solution of the chlorido-coordinated complexes **3** and **7** in 1:9 (v/v) MeOH/phosphate buffer of pH 7.4 containing 4 mM NaCl shows a relative decline in the intensity of the molecular-ion peak during the 24 h period (Figures S44−S49). ESI-MS of the iodido complex **8** shows a relatively higher population of the molecular-ion peak during the 24 h time period (Figures S50−S52). However, in a ESI-MS stock solution where the concentration of the sample is low (200 μM), the iodido complex **8** exchanges the

https://doi.org/10.1021/acs.inorgchem.1c02979
Inorg. Chem. 2021, 60, 18379−18394

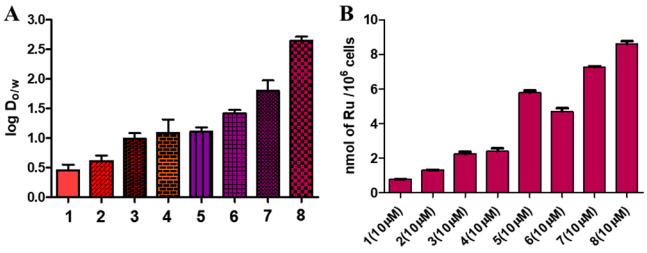

Figure 4. (A) Lipophilicity of metal complexes **1**−**8** in a 1:1 (v/v) *n*-octanol and water mixture at 37 °C. (B) Cellular accumulation study of a Ru^{II} complex (10 μM) in MDA-MB-231 cells.

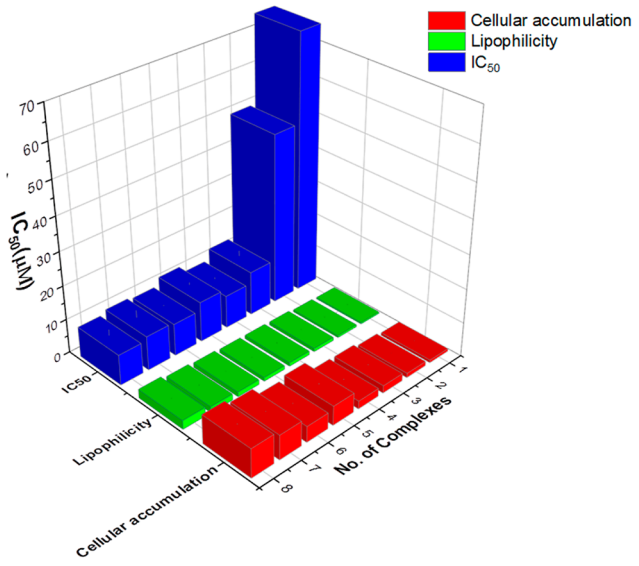

Figure 5. 3D correlation diagram of the cellular accumulation, lipophilicity, and IC_{50} values.

coordinated halide with chlorido at both 4 or 130 mM NaCl in the 24 h time period (Figures S50−S53).

Overall, the iodido complexes are more stable, but even the chlorido complexes are stable upon immediate monoaquation, and ca. 70% remains in solution even at 72 h. This is unlike our previous report, where the use of the bis-(pyrazolylbenzimidazole) ligand of 2,4-dimethylpyrazole with ruthenium(II)-*p*-cymene showed the chlorido complexes to be more stable.[65] The absence of a pyrazole group, the methyl substituents in the pyrazole motif, and the presence of a halide in the pyrazole have altered the electronic parameters, making the ruthenium(II) iodido coordination stronger. Thus, substitution by a halide in the 4 position of the pyrazole did not change the solution stability of the complexes significantly (less than a 10% change in aqueous stability), but it may be argued that the solubility of complexes **7** and **8** of the iodo-substituted **L4** is better with respect to the others in the same family presented here.

Determination of the Distribution Coefficient. Lipophilicity is an essential parameter for the determination of the drug-likeness of a new molecule.[91] According to the comprehensive medicinal chemistry database, pharmacophores generally should have lipophilicity values in the range from −0.4 to +5.6.[92] We knew that the chlorido complexes aquate and there is arene loss in a longer period, so it may be argued, what is the merit of the lipophilicity study? Yet, we studied the distribution coefficient (log $D_{o/w}$) because the equilibration is for a shorter period of time (6 h), and the partition coefficient trend is a good indication of the complex's ability to traverse across the membrane. The method adopted was the octanol−water shake-flask method as per the literature.[92] The data show that the lipophilicity increases with the introduction of halogen in the ligand (**L1**−**L4**) and alteration of the halogen coordinated to Ru^{II} (Figure 4A), with values increasing from ca. 0.5 in **1** to ca. 2.7 in **8**. The data were measured in an unbuffered aqueous medium, but the pH remained between 7.1 and 7.4. The iodido-coordinated complexes (**2**, **4**, **6**, and **8**) display higher lipophilicity values than their chlorido analogues (**1**, **3**, **5**, and **7**). The enhancement in the lipophilicity due to the incorporation of iodido coordination correlates well with our earlier results.[88,93] Similarly, introducing the halide into the ligand and increasing its size while keeping the chlorido coordination the same shows an increase in the lipophilicity from complexes **L1** to **L4** (**1** < **3** < **5** < **7**). The presence of 4-iodopyrazole in **L4** makes the respective metal complex **7** much more lipophilic than the iodido-coordinated **2**. Complex **8** has both the iodido-coordinated Ru^{II} and iodo-containing **L4**, displaying the highest lipophilicity of 2.64 ± 0.05 among the eight complexes.

Cytotoxicity Studies. *In vitro* cytotoxicity of all four ligands (**L1**−**L4**) and metal complexes (**1**−**8**) against the TNBC cell line MDA-MB-231 showed improvement in a cytotoxic dose of the metal complexes with the introduction of halides in their corresponding ligand compared to the metal complexes of an unsubstituted pyrazolylbenzimidazole ligand. A TNBC cell line was chosen because of its reluctance to respond to many therapeutic measures other than chemotherapy because of the absence of three primary targeting receptors (estrogen, progesterone, and HER2).[94] The TNBCs are known to have a very high relapse rate.[95] The ligands were designed as antiangiogenesis agents, so we also measured their standalone toxicity. The IC_{50} of **L1** is greater than 100 μM, and the IC_{50} of **L2**−**L4** is greater than 70 μM, suggesting lower *in vitro* toxicity of the ligands (Figure S58). However, we do not see more than 75% killing by the ligands alone even at higher doses (200 μM), so we could not determine the IC_{50} using the

Table 2. *In Vitro* Anticancer Activity of Complexes 1−8 in the Cancer Cell Line MDA-MB-231 under Normoxic Conditions after 72 h of Incubation with the Complex

	complexes								
	1	**2**	**3**	**4**	**5**	**6**	**7**	**8**	CDDP[b]
IC_{50} ± SD (μM)[a]	>75	>50	13.0 ± 1.6	9.7 ± 0.5	11.9 ± 0.7	9.5 ± 0.2	10.1 ± 2.2	9.0 ± 1.8	14.1 ± 0.5

[a]IC_{50} ± SD is determined by MTT assay in normoxia (~15% O_2). IC_{50} values were calculated by nonlinear four-parameter curve fitting in a dose-response inhibition−variable slope model using *GraphPad Prism*. SD = standard deviation. The indicative plots are provided in Figure S58. The data presented are the mean of at least three independent experiments; each concentration was assayed in triplicate in a single experiment. The statistical significance (P) of the data is >0.001 to <0.05. [b]CDDP = cisplatin.

https://doi.org/10.1021/acs.inorgchem.1c02979
Inorg. Chem. 2021, 60, 18379−18394

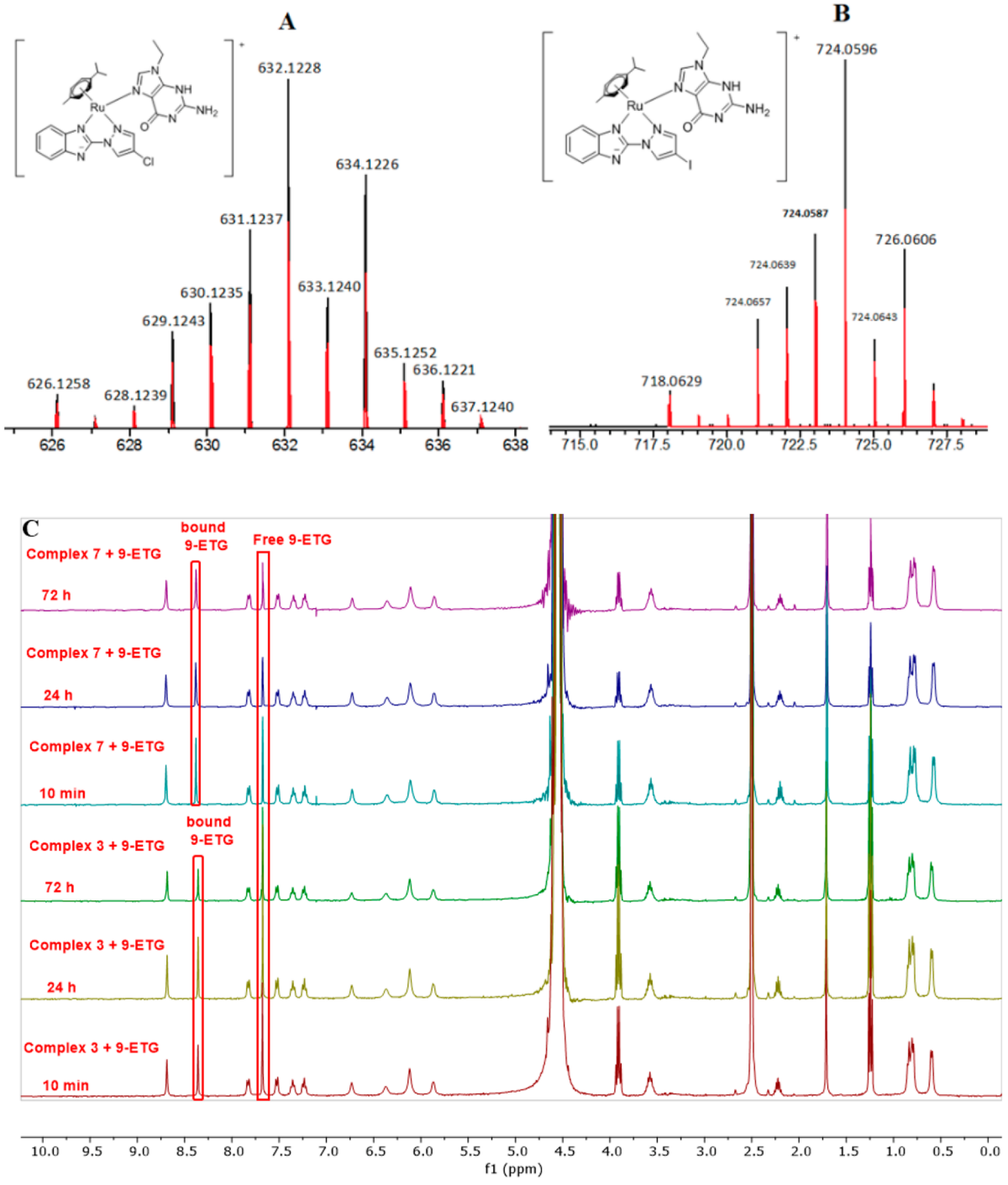

Figure 6. Interaction of complexes **3** and **7** with 9-EtG (2.5 equiv) in a 10 mM phosphate buffer containing 4 mM NaCl (pH* 7.4) shown in both ESI-MS and ^{1}H NMR: (A) 9-EtG-bound species with complex **3** recorded right after 5 min; (B) 9-EtG-bound species with complex **7** recorded right after 5 min. (C) ^{1}H NMR of complexes **3** and **7** with 9-EtG at different time intervals showing that the Ru center binds with 9-EtG.

curve-fitting process, and only the lower range is provided. Certainly, the results show that the ligand is not as toxic *in vitro* compared to their corresponding Ru^{II} complexes (Table 2). The solution stability study of the chlorido analogues (**3**, **5**, and **7**) suggests immediate aquation, and it is mostly the aquated complexes that are responsible for the cytotoxicity. Most of the iodido complexes (**2**, **4**, **6**, and **8**) exhibit higher toxicity than their respective chlorido analogues (**1**, **3**, **5**, and **7**). The major factors in the increase of the cytotoxicity of the iodido analogues may be the combination of higher lipophilicity and better stability, enabling better internalization of intact complexes in cells. The approximate 5-fold increase in the cytotoxicity of **3** compared to **1** suggests that the introduction of a halide in the 4 position of the pyrazole in **L2** has a strong impact on the cytotoxic efficacy, justifying the synthesis and study of various halide-substituted ligands and their corresponding complexes. Complex **8**, which has 4-iodopyrazole in the ligand (**L4**) instead of an unsubstituted pyrazole and Ru−I coordination, is at least 8 times more toxic than **1** with the unsubstituted pyrazole and Ru−Cl

https://doi.org/10.1021/acs.inorgchem.1c02979
Inorg. Chem. 2021, 60, 18379−18394

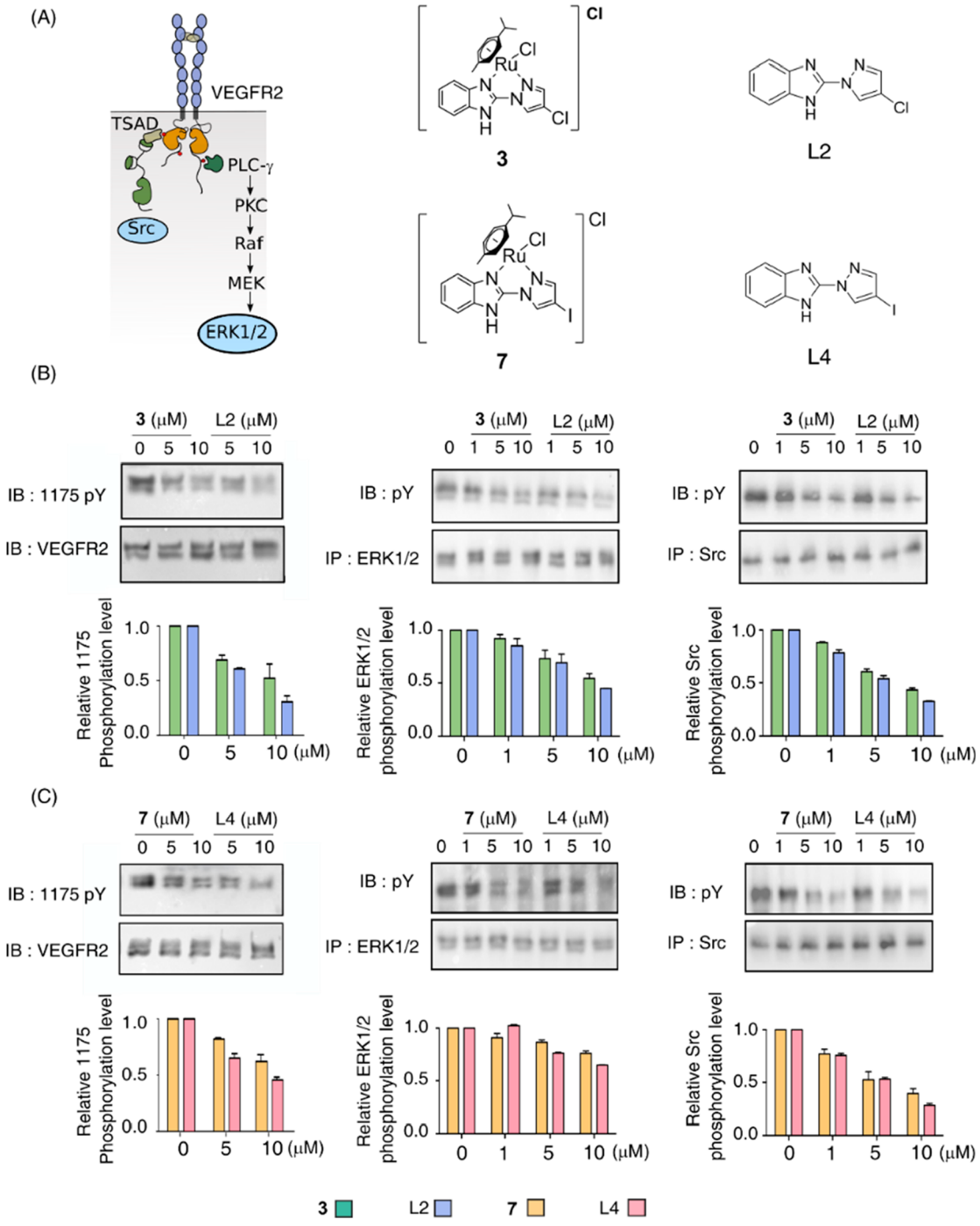

Figure 7. Effect of **L2**, **L4**, **3**, and **7** on the kinase activity in the MDA-MB-231 cell line. (A) Schematic representation of the VEGFR2 signaling pathway (left panel) and structural drawings of **L2**, **L4**, **3**, and **7** (right panel). (B and C) Representative Western blot strips of total VEGFR2, Y_{1175}-phosphorylated VEGFR2, ERK1/2, and Src, and phosphorylated ERK1/2 and Src after treatment with various concentrations of **L2**, **L4**, **3**, and **7**. The bar plots represent the quantification of Y1175 phosphorylation of VEGFR2 and the total phosphorylation level of immunoprecipitated Src and ERK1/2, indicating the concentration.

coordination. Complex **2** with **L1** and Ru−I coordination is also poor in cytotoxicity. Thus, **1** and **2**, with no halide in the ligand, have poor cytotoxic profiles compared to the rest of the family, which have either a Cl, Br, or I in the ligand by using a 4-halo-substituted pyrazole. While Ru−I coordination increased the stability, introducing an iodo in the ligand improved the cytotoxicity (Table 2). The ruthenium(II) *p*-cymene complex **3**, having 4-chloropyrazole and a Ru−Cl bond, displays toxicity similar to that of the 4-iodopyrazole-bearing **L4**-coordinated Ru−Cl or Ru−I complexes **7** and **8**. The use of 4-bromopyrazole (**5** and **6**) also led to improvement in the cytotoxicity profile compared with **1** and **2**. However, there is only a marginal difference in the cytotoxicity of **5** and **6** compared with the iodido-substituted **7** and **8**. Thus, although the introduction of the halide in the unsubstituted pyrazole increased the cytotoxicity, the change of

https://doi.org/10.1021/acs.inorgchem.1c02979
Inorg. Chem. 2021, 60, 18379−18394

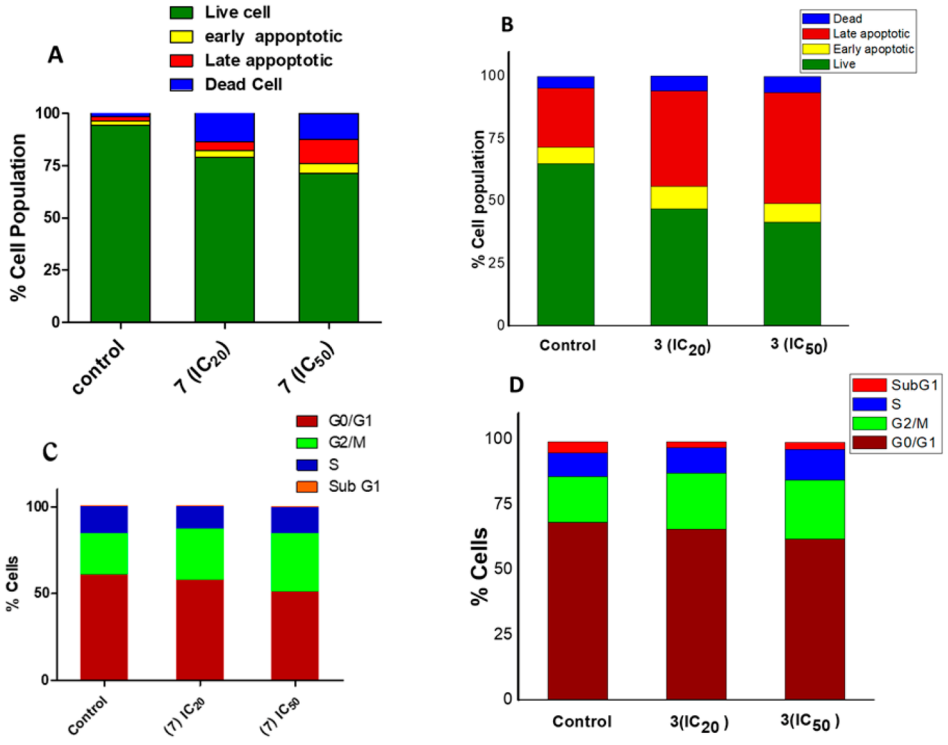

Figure 8. *In vitro* mechanistic analysis against MDA-MB-231 using flow cytometry: induction of apoptosis by complexes **7** (A) and **3** (B) in a dose-dependent (IC_{20} and IC_{50}) manner; cell cycle analysis of complexes **7** (C) and **3** (D) in a dose-dependent (IC_{20} and IC_{50}) manner.

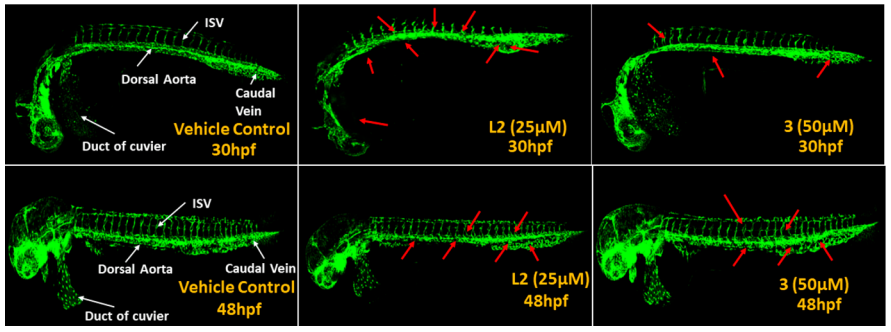

Figure 9. *In vivo* antiangiogenic activity of **L2** and **3** on Tg(Fli1:gfp) zebrafish at different time points. The white arrows demonstrate the GFP-expressing areas of interest (duct of Cuvier, dorsal aorta, ISVs, and caudal vein) in the vehicle control (0.2% DMSO), while the red arrows dictate the affected parts in treated samples.

Scheme 1. Synthetic Scheme of the Ligands L1−L4 and the Ru^{II} Complexes 1−8

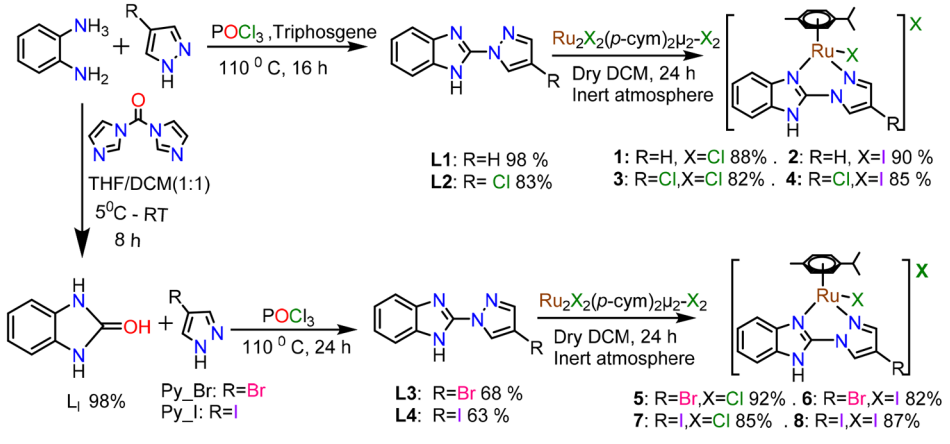

https://doi.org/10.1021/acs.inorgchem.1c02979
Inorg. Chem. 2021, 60, 18379−18394

the halide from chloride to iodide in the 4 position of the pyrazole showed less dose improvement in cytotoxicity profile. Thus, complexes **4** and **6**−**8** exhibit similar IC_{50} values in the range of 9−10 μM but are more toxic than cisplatin against the TNBC cell MDA-MB-231.[96]

Cellular Accumulation. We investigated the cellular ruthenium uptake to compare the internalization, lipophilicity, cytotoxicity, and stability, with a variation of the halide in the ligand and in coordination to the ruthenium(II) *p*-cymene. ICP-OES measured the Ru content (nmol of Ru per 10^6 cells) in MDA-MB-231 cells after 16 h of treatment with 10 μM **1**−**8**. The cellular Ru uptake data (Figure 4B) correlate well with the lipophilicity and cytotoxicity (Figure 5). There is an overall increase in cellular accumulation because of the introduction of halogens, which increase the bulk in the ligand system and coordinate with Ru^{II}. Thus, complex **8** has the highest accumulation, and complex **7** is the next closest, but **7** has poorer solution stability and is marginally less cytotoxic than **8**. Our observation is supported by similar results from earlier works with halogen-substituted hydroxyquinoline-based metal complexes.[97,98] Complexes **4** and **6** are quite efficient despite their low cellular accumulation and almost similar in cytotoxicity to **7** and **8**.

Pathways of Cytotoxicity. *Interaction with the Model Nucleobase 9-EtG.* $Ru^{II/III}$ complexes interact with both nucleobases and proteins.[28,29,97] We used complexes **3** and **7** as representatives to investigate the DNA interaction with the model nucleobase 9-EtG. The cytotoxicity data of the metal complexes emphasized the importance of halide substitution in the pyrazolylbenzimidazole ligand system. We found that the toxicities of complexes **3**−**8** are similar. In addition, ligands **L2** and **L4** also showed better toxicity than the other two ligands, so complexes of the corresponding ligands **3** and **7**, which aquate well, were taken for the 9-EtG binding studies. We observed that the complexes rapidly bind to 9-EtG (2.5 equiv) within 5−10 min of addition, confirmed by ^{1}H NMR (Figure 6C) and ESI-HRMS (Figure 6A,B). A substantial downfield shift of the H8 proton was observed in ^{1}H NMR after 10 min of addition (Figures 6C and S42 and S43). This downfield shift confirms that 9-EtG binds to Ru^{II} in the complex.[98] The ESI-HRMS studies showed the 9-EtG-bound adduct for **3** and **7** at m/z 632.1263 (calcd 632.1222) and 724.0592 (calcd 724.0578), respectively, after 24 h of incubation with 9-EtG (Figures S54−S57).

VEGFR2 Inhibition: Effect on the Kinase Signaling Pathway. The Ru^{II} complexes demonstrate 9-EtG binding capability and much higher cytotoxicity than the ligands. The ligands were designed as the organic-directing groups to inhibit VEGFR2 phosphorylation. The effect of the ligands and metal complexes on phosphorylation of the tyrosine, Y_{1175}, showed the signature of inhibition of VEGFR2 signaling activity.[99] Activation of VEGFR2 by $VEGF_{165a}$ in the MDA-MB-231 cell line, followed by treatment with two doses (5 and 10 μM) of **L2**, **L4**, **3**, and **7**, showed that the ligands and corresponding complexes inhibit the phosphorylation at Y_{1175}. The ligands are responsible for inhibiting VEGFR2 phosphorylation, and the quantitation data from Western blots suggest that **L2** and **L4** display similar activities, which are higher than their corresponding metal complexes **3** and **7** (Figures 7 and S59). It is important to note here that the ligands have IC_{50} values greater than 70 μM but they inhibit VEGFR2 phosphorylation at 5−10 μM. Thus, the cellular proliferation under *in vitro* conditions may not strongly depend on the VEGFR2 inhibition.[65,100] Nevertheless, the inhibitory activity is suggesting that the ligand design has successfully rendered pyrazolylbenzimidazole-based ruthenium(II) *p*-cymene complexes, inhibiting VEGFR2 phosphorylation.

The inhibition of phosphorylation was also found for other related kinases capable of acting downstream of VEGFR2 and independently, viz., ERK1/2 and Src.[101,102] **L2**, **L4**, **3**, and **7** exhibit less effect on ERK1/2 and more prominently affect Src phosphorylation. Thus, the results show that **L2**, **L4**, **3**, and **7** inhibit VEGFR2 phosphorylation and affect the downstream Src signaling pathway more prominently (Figures 7 and S59).

Treatment of the MDA-MB-231 cells with complexes **3** and **7** shows that they arrest the cell cycle in the G2/M phase at IC_{20} and IC_{50} values (Figures 8C,D and S60) and induce apoptosis (Annexin V-PE/7-AAD dual staining assay). The late apoptotic cell population increases compared to the control for IC_{50} doses of **3** and **7**, respectively, upon 8 h of drug exposure (Figures 8A,B and S61).

In vivo Antiangiogenesis on Zebrafish. The zebrafish (*Danio rerio*) made an appearance as an ideal vertebrate model to study numerous biological processes in the past decade because their semitransparent nature facilitates visualization and they have ca. 70% similarity with the human genome. Their high fecundity rates and the possibility for external fertilization and rapid growth and development ascribe them to an important embroyological model. Vascular studies on zebrafish provide insight into vasculogenesis and angiogenesis,[103] and their semitransparent nature allows excellent optical clarity.[104] In order to find out whether our *in vitro* inhibition of VEGFR2 phosphorylation translates to anti-angiogenic activity *in vivo*, we used transgenic Tg(fli1:gfp) zebrafish expressing the GFP on endothelial cells during development as a tool to anticipate developing blood vessels. Chloride-conjugated ligand **L2** and its corresponding chlorido metal complex **3** were chosen as representative compounds for this experiment because complexes **3**−**8** showed cytotoxicity in a similar range and **L2** and **3** also showed good activity against phosphorylation of VEGFR2. Developing embryos treated for 12 h with either **L2** (25 μM) or **3** (50 μM) at 14 hpf, followed by drug removal, showed that at 30 hpf there is no formation of the duct of Cuvier, defects in the formation of the ISVs, caudal vein, and development of dorsal aorta in comparison with development with the vehicle control (0.2% DMSO). However, the effect is more prominent in **L2**-treated zebrafish than **3**. There is a partial reversal of the effect at 48 hpf after drug removal, but a persistent effect has been observed in various areas in the caudal vein and ISVs. We also noticed that the mortality rate is zero because there was no death in the experiments, taking (25 × 3) zebrafish at given doses. Thus, the ligands are mostly responsible for the antiangiogenic activity of the complexes based on our *in vitro* and *in vivo* findings.

CONCLUSIONS

The organometallic Ru(II) complex of *N*,*N*-chelating pyrazolylbenzimidazole ligands inhibit phosphorylation of VEGFR2 in $VEGF_{165a}$-activated MDA-MB-231. The iodido-coordinated complexes (**2**, **4**, **6**, and **8**) are more resistant toward aquation at physiological conditions (pH 7.4, 4 mM Cl^-). The complexes display the potential ability to bind to DNA through the Ru^{II} center, whereas the ligands assist VEGFR2 inhibition. Complexes **3**, **7** and their respective ligands (**L2** and **L4**) inhibit the VEGFR2 signaling pathway,

https://doi.org/10.1021/acs.inorgchem.1c02979
Inorg. Chem. 2021, 60, 18379−18394

downregulating phosphorylated VEGFR2, ERK1/2, and Src. Inhibition by the ligand is observed at nontoxic *in vitro* doses in comparison to the metal complex. The time-dependent 9-EtG binding via ^{1}H NMR shows that DNA may be a target for the metal complexes, providing a reason for their higher cytotoxicities. The *in vivo* studies on the Tg(fli1:gfp) zebrafish model show that antiangiogenic activity is observed in zebrafish treated with specific doses of **L2** and **3** and the effect is more distinct in zebrafish treated with **L2** than **3**. In fact, **3**-treated zebrafish show rather poor effects on the antiangiogenic activity. The scope of further functionalization of the halo derivatives of pyrazolylbenzimidazole ligands provides an excellent platform to tailor more potent VEGFR2-inhibiting metal complexes in future.

■ ASSOCIATED CONTENT

Supporting Information

The Supporting Information is available free of charge at https://pubs.acs.org/doi/10.1021/acs.inorgchem.1c02979.

NMR spectra (^{1}H and ^{13}C) of ligands (Figures S1−S8) and complexes (Figures S9−S32; ^{1}H, ^{13}C, and HMQC), UV−vis spectra of all of the complexes (Figure S33), lattice packing and crystallographic parameter table (Figure S34 and Table S1), hydrolysis and 9-EtG binding of the complexes (**1**−**8**) by ^{1}H NMR (Figures S35−S43) and ESI-MS (Figures S44−S57), IC_{50} plots of all complexes and ligands (Figure S58), uncropped Western blot (Figure S59), and flow cytometric determination of the cell cycle and apoptosis (Figures S60 and S61) (PDF)

Accession Codes

CCDC 2087583 and 2087584 contain the supplementary crystallographic data for this paper. These data can be obtained free of charge via www.ccdc.cam.ac.uk/data_request/cif, or by emailing data_request@ccdc.cam.ac.uk, or by contacting The Cambridge Crystallographic Data Centre, 12 Union Road, Cambridge CB2 1EZ, UK; fax: +44 1223 336033.

■ AUTHOR INFORMATION

Corresponding Author

Arindam Mukherjee − *Department of Chemical Sciences and Centre for Advanced Functional Materials, Indian Institute of Science Education and Research (IISER) Kolkata, Mohanpur 741246, India;* orcid.org/0000-0001-9545-8628; Email: a.mukherjee@iiserkol.ac.in

Authors

Ayan Chakraborty − *Department of Chemical Sciences, Indian Institute of Science Education and Research (IISER) Kolkata, Mohanpur 741246, India*

Souryadip Roy − *Department of Chemical Sciences, Indian Institute of Science Education and Research (IISER) Kolkata, Mohanpur 741246, India*

Manas Pratim Chakraborty − *Department of Biological Sciences, Indian Institute of Science Education and Research (IISER) Kolkata, Mohanpur 741246, India*

Shantanu Saha Roy − *National Institute of Biomedical Genomics, Kalyani 741251, India*

Kallol Purkait − *Department of Chemical Sciences, Indian Institute of Science Education and Research (IISER) Kolkata, Mohanpur 741246, India*

Tuhin Subhra Koley − *Department of Chemical Sciences, Indian Institute of Science Education and Research (IISER) Kolkata, Mohanpur 741246, India*

Rahul Das − *Department of Biological Sciences and Centre for Advanced Functional Materials, Indian Institute of Science Education and Research (IISER) Kolkata, Mohanpur 741246, India;* orcid.org/0000-0001-7841-8229

Moulinath Acharya − *National Institute of Biomedical Genomics, Kalyani 741251, India*

Complete contact information is available at: https://pubs.acs.org/10.1021/acs.inorgchem.1c02979

Author Contributions

†These authors contributed equally to this paper.

Author Contributions

The project was designed by A.M. A.C. performed the synthesis, characterization, NMR data for solution stability, lipophilicity, ICP-OES, cell cycle, and apoptosis. S.R. performed all of the NMR data for solution stability at 37 °C, 9-EtG reactivity, *in vitro* cytotoxicity data, cell cycle, and apoptosis, treated cells for immunoblots, helped in the *in vivo* zebrafish experiments, coordinated the manuscript writing, and verified the cell cycle and apoptosis data carried out by A.C. K.P. performed single-crystal X-ray crystallography and solved the structures. T.S.K. completed and verified the ESI-MS stability studies. M.P.C. carried out all of the kinase assays and coordinated manuscript writing, supervised by R.D. S.S.R. performed the *in vivo* experimentation on zebrafish under the supervision of M.A. A.M. supervised the overall work. All authors have approved the final version of the manuscript.

Notes

The authors declare no competing financial interest.

■ ACKNOWLEDGMENTS

We earnestly acknowledge SERB for financial support via Project EMR/2017/002324. We also thank IISER Kolkata for infrastructural and financial support. The authors acknowledge NIBMG Kalyani for providing intramural support to the NIBMG Zebrafish facility. A.C. thanks UGC, S.R. thanks Inspire, M.P.C. thanks CSIR, K.P. thanks UGC, and T.S.K. thanks IISER Kolkata for providing their research fellowships. The authors thank Tamal Ghosh for his help with flow cytometry.

■ REFERENCES

(1) Ndagi, U.; Mhlongo, N.; Soliman, M. E. Metal complexes in cancer therapy - an update from drug design perspective. *Drug Des., Dev. Ther.* **2017**, *11*, 599−616.

(2) Florea, A.-M.; Buesselberg, D. Cisplatin as an anti-tumor drug: cellular mechanisms of activity, drug resistance and induced side effects. *Cancers* **2011**, *3*, 1351−1371.

(3) Kelland, L. The resurgence of platinum-based cancer chemotherapy. *Nat. Rev. Cancer* **2007**, *7* (8), 573−584.

(4) Johnstone, T. C.; Suntharalingam, K.; Lippard, S. J. The Next Generation of Platinum Drugs: Targeted Pt(II) Agents, Nanoparticle Delivery, and Pt(IV) Prodrugs. *Chem. Rev.* **2016**, *116* (5), 3436−3486.

(5) Zeng, L.; Gupta, P.; Chen, Y.; Wang, E.; Ji, L.; Chao, H.; Chen, Z.-S. The development of anticancer ruthenium(II) complexes: from single molecule compounds to nanomaterials. *Chem. Soc. Rev.* **2017**, *46* (19), 5771−5804.

(6) Thota, S.; Rodrigues, D. A.; Crans, D. C.; Barreiro, E. J. Ru(II) Compounds: Next-Generation Anticancer Metallotherapeutics? *J. Med. Chem.* **2018**, *61* (14), 5805−5821.

(7) Chitambar, C. R. Gallium-containing anticancer compounds. *Future Med. Chem.* **2012**, *4* (10), 1257−1272.
(8) Timerbaev, A. R. Advances in developing tris(8-quinolinolato)-gallium(III) as an anticancer drug: critical appraisal and prospects. *Metallomics* **2009**, *1* (3), 193−198.
(9) Plaks, V.; Koudinova, N.; Nevo, U.; Pinthus, J. H.; Kanety, H.; Eshhar, Z.; Ramon, J.; Scherz, A.; Neeman, M.; Salomon, Y. Photodynamic therapy of established prostatic adenocarcinoma with TOOKAD: a biphasic apparent diffusion coefficient change as potential early MRI response marker. *Neoplasia* **2004**, *6* (3), 224−33.
(10) Azzouzi, A. R.; Lebdai, S.; Benzaghou, F.; Stief, C. Vascular-targeted photodynamic therapy with TOOKAD® Soluble in localized prostate cancer: standardization of the procedure. *World J. Urol.* **2015**, *33* (7), 937−44.
(11) Aird, R. E.; Cummings, J.; Ritchie, A. A.; Muir, M.; Morris, R. E.; Chen, H.; Sadler, P. J.; Jodrell, D. I. In vitro and in vivo activity and cross resistance profiles of novel ruthenium (II) organometallic arene complexes in human ovarian cancer. *Br. J. Cancer* **2002**, *86* (10), 1652−1657.
(12) Han Ang, W.; Dyson, P. J. Classical and non-classical ruthenium-based anticancer drugs: towards targeted chemotherapy. *Eur. J. Inorg. Chem.* **2006**, *2006* (20), 4003−4018.
(13) Bruijnincx, P. C. A.; Sadler, P. J. New trends for metal complexes with anticancer activity. *Curr. Opin. Chem. Biol.* **2008**, *12* (2), 197−206.
(14) Leijen, S.; Burgers, S. A.; Baas, P.; Pluim, D.; Tibben, M.; van Werkhoven, E.; Alessio, E.; Sava, G.; Beijnen, J. H.; Schellens, J. H. M. Phase I/II study with ruthenium compound NAMI-A and gemcitabine in patients with non-small cell lung cancer after first line therapy. *Invest. New Drugs* **2015**, *33* (1), 201−214.
(15) Wernitznig, D.; Kiakos, K.; Del Favero, G.; Harrer, N.; Machat, H.; Osswald, A.; Jakupec, M. A.; Wernitznig, A.; Sommergruber, W.; Keppler, B. K. First-in-class ruthenium anticancer drug (KP1339/IT-139) induces an immunogenic cell death signature in colorectal spheroids in vitro†. *Metallomics* **2019**, *11* (6), 1044−1048.
(16) Dickson, N. R.; Jones, S. F.; Burris, H. A.; Ramanathan, R. K.; Weiss, G. J.; Infante, J. R.; Bendell, J. C.; McCulloch, W.; Von Hoff, D. D. A phase I dose-escalation study of NKP-1339 in patients with advanced solid tumors refractory to treatment. *J. Clin. Oncol.* **2011**, *29*, 2607−2607.
(17) Trondl, R.; Heffeter, P.; Kowol, C. R.; Jakupec, M. A.; Berger, W.; Keppler, B. K. NKP-1339, the first ruthenium-based anticancer drug on the edge to clinical application. *Chem. Sci.* **2014**, *5* (8), 2925−2932.
(18) Shi, G.; Monro, S.; Hennigar, R.; Colpitts, J.; Fong, J.; Kasimova, K.; Yin, H.; DeCoste, R.; Spencer, C.; Chamberlain, L.; Mandel, A.; Lilge, L.; McFarland, S. A. Ru(II) dyads derived from α-oligothiophenes: A new class of potent and versatile photosensitizers for PDT. *Coord. Chem. Rev.* **2015**, *282*−*283*, 127−138.
(19) Chen, Q.; Ramu, V.; Aydar, Y.; Groenewoud, A.; Zhou, X. Q.; Jager, M. J.; Cole, H.; Cameron, C. G.; McFarland, S. A.; Bonnet, S.; Snaar-Jagalska, B. E. TLD1433 Photosensitizer Inhibits Conjunctival Melanoma Cells in Zebrafish Ectopic and Orthotopic Tumour Models. *Cancers* **2020**, *12* (3), 587.
(20) Steel, T. R.; Walsh, F.; Wieczorek-Błauż, A.; Hanif, M.; Hartinger, C. G. Monodentately-coordinated bioactive moieties in multimodal half-sandwich organoruthenium anticancer agents. *Coord. Chem. Rev.* **2021**, *439*, 213890.
(21) Murray, B. S.; Babak, M. V.; Hartinger, C. G.; Dyson, P. J. The development of RAPTA compounds for the treatment of tumors. *Coord. Chem. Rev.* **2016**, *306*, 86−114.
(22) Peacock, A. F. A.; Sadler, P. J. Medicinal Organometallic Chemistry: Designing Metal Arene Complexes as Anticancer Agents. *Chem. - Asian J.* **2008**, *3* (11), 1890−1899.
(23) Zhang, P.; Sadler, P. J. Advances in the design of organometallic anticancer complexes. *J. Organomet. Chem.* **2017**, *839*, 5−14.
(24) Soldevila-Barreda, J. J.; Romero-Canelón, I.; Habtemariam, A.; Sadler, P. J. Transfer hydrogenation catalysis in cells as a new approach to anticancer drug design. *Nat. Commun.* **2015**, *6* (1), 6582.
(25) Morris, R. E.; Aird, R. E.; del Socorro Murdoch, P.; Chen, H.; Cummings, J.; Hughes, N. D.; Parsons, S.; Parkin, A.; Boyd, G.; Jodrell, D. I.; Sadler, P. J. Inhibition of Cancer Cell Growth by Ruthenium(II) Arene Complexes. *J. Med. Chem.* **2001**, *44* (22), 3616−3621.
(26) Meier-Menches, S. M.; Gerner, C.; Berger, W.; Hartinger, C. G.; Keppler, B. K. Structure−activity relationships for ruthenium and osmium anticancer agents − towards clinical development. *Chem. Soc. Rev.* **2018**, *47* (3), 909−928.
(27) Brabec, V.; Kasparkova, J. Ruthenium coordination compounds of biological and biomedical significance. DNA binding agents. *Coord. Chem. Rev.* **2018**, *376*, 75−94.
(28) Kenny, R. G.; Marmion, C. J. Toward Multi-Targeted Platinum and Ruthenium Drugs—A New Paradigm in Cancer Drug Treatment Regimens? *Chem. Rev.* **2019**, *119* (2), 1058−1137.
(29) Štarha, P.; Trávníček, Z. Non-platinum complexes containing releasable biologically active ligands. *Coord. Chem. Rev.* **2019**, *395*, 130−145.
(30) Rohrabaugh, T. N., Jr.; Rohrabaugh, A. M.; Kodanko, J. J.; White, J. K.; Turro, C. Photoactivation of imatinib-antibody conjugate using low-energy visible light from Ru(II)-polypyridyl cages. *Chem. Commun.* **2018**, *54* (41), 5193−5196.
(31) Du, J.; Zhang, E.; Zhao, Y.; Zheng, W.; Zhang, Y.; Lin, Y.; Wang, Z.; Luo, Q.; Wu, K.; Wang, F. Discovery of a dual-targeting organometallic ruthenium complex with high activity inducing early stage apoptosis of cancer cells. *Metallomics* **2015**, *7* (12), 1573−1583.
(32) Qiu, K.; Chen, Y.; Rees, T. W.; Ji, L.; Chao, H. Organelle-targeting metal complexes: From molecular design to bio-applications. *Coord. Chem. Rev.* **2019**, *378*, 66−86.
(33) Schmid, W. F.; John, R. O.; Muehlgassner, G.; Heffeter, P.; Jakupec, M. A.; Galanski, M.; Berger, W.; Arion, V. B.; Keppler, B. K. Metal-Based Paullones as Putative CDK Inhibitors for Antitumor Chemotherapy. *J. Med. Chem.* **2007**, *50* (25), 6343−6355.
(34) Maksimoska, J.; Feng, L.; Harms, K.; Yi, C.; Kissil, J.; Marmorstein, R.; Meggers, E. Targeting Large Kinase Active Site with Rigid, Bulky Octahedral Ruthenium Complexes. *J. Am. Chem. Soc.* **2008**, *130* (47), 15764−15765.
(35) Fontanella, C.; Ongaro, E.; Bolzonello, S.; Guardascione, M.; Fasola, G.; Aprile, G. Clinical advances in the development of novel VEGFR2 inhibitors. *Ann. Transl. Med.* **2014**, *2* (12), 123-1−123-10.
(36) Matsui, J.; Funahashi, Y.; Uenaka, T.; Watanabe, T.; Tsuruoka, A.; Asada, M. Multi-Kinase Inhibitor E7080 Suppresses Lymph Node and Lung Metastases of Human Mammary Breast Tumor MDA-MB-231 via Inhibition of Vascular Endothelial Growth Factor-Receptor (VEGF-R) 2 and VEGF-R3 Kinase. *Clin. Cancer Res.* **2008**, *14* (17), 5459−5465.
(37) Li, M.-y.; Lv, Y.-c.; Tong, L.-j.; Peng, T.; Qu, R.; Zhang, T.; Sun, Y.-m.; Chen, Y.; Wei, L.-x.; Geng, M.-y.; Duan, W.-h.; Xie, H.; Ding, J. DW10075, a novel selective and small-molecule inhibitor of VEGFR, exhibits antitumor activities both in vitro and in vivo. *Acta Pharmacol. Sin.* **2016**, *37* (3), 398−407.
(38) Aprile, G.; Bonotto, M.; Ongaro, E.; Pozzo, C.; Giuliani, F. Critical Appraisal of Ramucirumab (IMC-1121B) for Cancer Treatment: From Benchside to Clinical Use. *Drugs* **2013**, *73* (18), 2003−2015.
(39) Xie, C.; Wan, X.; Quan, H.; Zheng, M.; Fu, L.; Li, Y.; Lou, L. Preclinical characterization of anlotinib, a highly potent and selective vascular endothelial growth factor receptor-2 inhibitor. *Cancer Sci.* **2018**, *109* (4), 1207−1219.
(40) Xie, P.; Williams, D. S.; Atilla-Gokcumen, G. E.; Milk, L.; Xiao, M.; Smalley, K. S. M.; Herlyn, M.; Meggers, E.; Marmorstein, R. Structure-Based Design of an Organoruthenium Phosphatidylinositol-3-kinase Inhibitor Reveals a Switch Governing Lipid Kinase Potency and Selectivity. *ACS Chem. Biol.* **2008**, *3* (5), 305−316.
(41) Chen, T.; Dong, J.; Zhou, H.; Deng, X.; Li, R.; Chen, N.; Luo, M.; Li, Y.; Wu, J.; Wang, L. Glycation of fibronectin inhibits VEGF-induced angiogenesis by uncoupling VEGF receptor-2-c-Src crosstalk. *J. Cell. Mol. Med.* **2020**, *24* (16), 9154−9164.

https://doi.org/10.1021/acs.inorgchem.1c02979
Inorg. Chem. 2021, 60, 18379−18394

(42) Jiang, J.-H.; Pi, J.; Cai, J.-Y. Oridonin exhibits anti-angiogenic activity in human umbilical vein endothelial cells by inhibiting VEGF-induced VEGFR-2 signaling pathway. *Pathol., Res. Pract.* **2020**, *216* (8), 153031.
(43) Bang, Y.-J.; Kang, Y.-K.; Kang, W. K.; Boku, N.; Chung, H. C.; Chen, J.-S.; Doi, T.; Sun, Y.; Shen, L.; Qin, S.; Ng, W.-T.; Tursi, J. M.; Lechuga, M. J.; Lu, D. R.; Ruiz-Garcia, A.; Sobrero, A. Phase II study of sunitinib as second-line treatment for advanced gastric cancer. *Invest. New Drugs* **2011**, *29* (6), 1449−1458.
(44) Xie, H.; Lafky, J. M.; Morlan, B. W.; Stella, P. J.; Dakhil, S. R.; Gross, G. G.; Loui, W. S.; Hubbard, J. M.; Alberts, S. R.; Grothey, A. Dual VEGF inhibition with sorafenib and bevacizumab as salvage therapy in metastatic colorectal cancer: results of the phase II North Central Cancer Treatment Group study N054C (Alliance). *Ther. Adv. Med. Oncol.* **2020**, *12*, 1758835920910913.
(45) Fan, G.; Wei, X.; Xu, X. Is the era of sorafenib over? A review of the literature. *Ther. Adv. Med. Oncol.* **2020**, *12*, 1758835920927602.
(46) Kim, R. D.; Sanoff, H. K.; Poklepovic, A. S.; Soares, H.; Kim, J.; Lyu, J.; Liu, Y.; Nixon, A. B.; Kim, D. W. A multi-institutional phase 2 trial of regorafenib in refractory advanced biliary tract. *Cancer* **2020**, *126* (15), 3464−3470.
(47) Kawazoe, A.; Fukuoka, S.; Nakamura, Y.; Kuboki, Y.; Wakabayashi, M.; Nomura, S.; Mikamoto, Y.; Shima, H.; Fujishiro, N.; Higuchi, T.; Sato, A.; Kuwata, T.; Shitara, K. Lenvatinib plus pembrolizumab in patients with advanced gastric cancer in the first-line or second-line setting (EPOC1706): an open-label, single-arm, phase 2 trial. *Lancet Oncol.* **2020**, *21* (8), 1057−1065.
(48) Cai, Z.-w.; Zhang, Y.; Borzilleri, R. M.; Qian, L.; Barbosa, S.; Wei, D.; Zheng, X.; Wu, L.; Fan, J.; Shi, Z.; Wautlet, B. S.; Mortillo, S.; Jeyaseelan, R.; Kukral, D. W.; Kamath, A.; Marathe, P.; D'Arienzo, C.; Derbin, G.; Barrish, J. C.; Robl, J. A.; Hunt, J. T.; Lombardo, L. J.; Fargnoli, J.; Bhide, R. S. Discovery of Brivanib Alaninate ((S)-((R)-1-(4-(4-Fluoro-2-methyl-1H-indol-5-yloxy)-5-methylpyrrolo[2,1-f]-[1,2,4]triazin-6-yloxy)propan-2-yl)2-aminopropanoate), A Novel Prodrug of Dual Vascular Endothelial Growth Factor Receptor-2 and Fibroblast Growth Factor Receptor-1 Kinase Inhibitor (BMS-540215). *J. Med. Chem.* **2008**, *51* (6), 1976−1980.
(49) Boyer, S. J. Small molecule inhibitors of KDR (VEGFR-2) kinase: an overview of structure activity relationships. *Curr. Top. Med. Chem.* **2002**, *2* (9), 973−1000.
(50) Potashman, M. H.; Bready, J.; Coxon, A.; DeMelfi, T. M., Jr.; DiPietro, L.; Doerr, N.; Elbaum, D.; Estrada, J.; Gallant, P.; Germain, J.; Gu, Y.; Harmange, J.-C.; Kaufman, S. A.; Kendall, R.; Kim, J. L.; Kumar, G. N.; Long, A. M.; Neervannan, S.; Patel, V. F.; Polverino, A.; Rose, P.; Van der Plas, S.; Whittington, D.; Zanon, R.; Zhao, H. Design, Synthesis, and Evaluation of Orally Active Benzimidazoles and Benzoxazoles as Vascular Endothelial Growth Factor-2 Receptor Tyrosine Kinase Inhibitors. *J. Med. Chem.* **2007**, *50* (18), 4351−4373.
(51) Hasegawa, M.; Nishigaki, N.; Washio, Y.; Kano, K.; Harris, P. A.; Sato, H.; Mori, I.; West, R. I.; Shibahara, M.; Toyoda, H.; Wang, L.; Nolte, R. T.; Veal, J. M.; Cheung, M. Discovery of Novel Benzimidazoles as Potent Inhibitors of TIE-2 and VEGFR-2 Tyrosine Kinase Receptors. *J. Med. Chem.* **2007**, *50* (18), 4453−4470.
(52) Abdel-Mohsen, H. T.; Abdullaziz, M. A.; El Kerdawy, A. M.; Ragab, F. A. F.; Flanagan, K. J.; Mahmoud, A. E. E.; Ali, M. M.; El Diwani, H. I.; Senge, M. O. Targeting receptor tyrosine kinase VEGFR-2 in hepatocellular cancer: rational design, synthesis and biological evaluation of 1,2-disubstituted benzimidazoles. *Molecules* **2020**, *25* (4), 770.
(53) Aziz, M. A.; Serya, R. A. T.; Lasheen, D. S.; Abdel-Aziz, A. K.; Esmat, A.; Mansour, A. M.; Singab, A. N. B.; Abouzid, K. A. M. Discovery of Potent VEGFR-2 Inhibitors based on Furopyrimidine and Thienopyrimidne Scaffolds as Cancer Targeting Agents. *Sci. Rep.* **2016**, *6*, 24460.
(54) McTigue, M.; Murray, B. W.; Chen, J. H.; Deng, Y.-L.; Solowiej, J.; Kania, R. S. Molecular conformations, interactions, and properties associated with drug efficiency and clinical performance among VEGFR TK inhibitors. *Proc. Natl. Acad. Sci. U. S. A.* **2012**, *109* (45), 18281−18289.
(55) Rydén, L.; Jirström, K.; Haglund, M.; Stål, O.; Fernö, M. Epidermal growth factor receptor and vascular endothelial growth factor receptor 2 are specific biomarkers in triple-negative breast cancer. Results from a controlled randomized trial with long-term follow-up. *Breast Cancer Res. Treat.* **2010**, *120* (2), 491−8.
(56) Isakoff, S. J. Triple-negative breast cancer: role of specific chemotherapy agents. *Cancer J.* **2010**, *16* (1), 53−61.
(57) Pandy, J. G. P.; Balolong-Garcia, J. C.; Cruz-Ordinario, M. V. B.; Que, F. V. F. Triple negative breast cancer and platinum-based systemic treatment: a meta-analysis and systematic review. *BMC Cancer* **2019**, *19* (1), 1065.
(58) Poggio, F.; Bruzzone, M.; Ceppi, M.; Pondé, N. F.; La Valle, G.; Del Mastro, L.; de Azambuja, E.; Lambertini, M. Platinum-based neoadjuvant chemotherapy in triple-negative breast cancer: a systematic review and meta-analysis. *Ann. Oncol.* **2018**, *29* (7), 1497−1508.
(59) Liao, M.; Zhang, J.; Wang, G.; Wang, L.; Liu, J.; Ouyang, L.; Liu, B. Small-Molecule Drug Discovery in Triple Negative Breast Cancer: Current Situation and Future Directions. *J. Med. Chem.* **2021**, *64* (5), 2382−2418.
(60) Berndsen, R. H.; Weiss, A.; Abdul, U. K.; Wong, T. J.; Meraldi, P.; Griffioen, A. W.; Dyson, P. J.; Nowak-Sliwinska, P. Combination of ruthenium(II)-arene complex [Ru(η^6-p-cymene)Cl2(pta)] (RAPTA-C) and the epidermal growth factor receptor inhibitor erlotinib results in efficient angiostatic and antitumor activity. *Sci. Rep.* **2017**, *7* (1), 43005.
(61) Du, J.; Kang, Y.; Zhao, Y.; Zheng, W.; Zhang, Y.; Lin, Y.; Wang, Z.; Wang, Y.; Luo, Q.; Wu, K.; Wang, F. Synthesis, Characterization, and in Vitro Antitumor Activity of Ruthenium(II) Polypyridyl Complexes Tethering EGFR-Inhibiting 4-Anilinoquinazolines. *Inorg. Chem.* **2016**, *55* (9), 4595−4605.
(62) Yang, M.; Bierbach, U. Metal-Containing Pharmacophores in Molecularly Targeted Anticancer Therapies and Diagnostics. *Eur. J. Inorg. Chem.* **2017**, *2017* (12), 1561−1572.
(63) Anand, R.; Maksimoska, J.; Pagano, N.; Wong, E. Y.; Gimotty, P. A.; Diamond, S. L.; Meggers, E.; Marmorstein, R. Toward the Development of a Potent and Selective Organoruthenium Mammalian Sterile 20 Kinase Inhibitor. *J. Med. Chem.* **2009**, *52* (6), 1602−1611.
(64) Feng, L.; Geisselbrecht, Y.; Blanck, S.; Wilbuer, A.; Atilla-Gokcumen, G. E.; Filippakopoulos, P.; Kraling, K.; Celik, M. A.; Harms, K.; Maksimoska, J.; Marmorstein, R.; Frenking, G.; Knapp, S.; Essen, L.-O.; Meggers, E. Structurally Sophisticated Octahedral Metal Complexes as Highly Selective Protein Kinase Inhibitors. *J. Am. Chem. Soc.* **2011**, *133* (15), 5976−5986.
(65) Bhattacharyya, S.; Purkait, K.; Mukherjee, A. Ruthenium(II) p-cymene complexes of a benzimidazole-based ligand capable of VEGFR2 inhibition: hydrolysis, reactivity and cytotoxicity studies. *Dalton Trans.* **2017**, *46* (26), 8539−8554.
(66) Luo, Z.; Yu, L.; Yang, F.; Zhao, Z.; Yu, B.; Lai, H.; Wong, K.-H.; Ngai, S.-M.; Zheng, W.; Chen, T. Ruthenium polypyridyl complexes as inducer of ROS-mediated apoptosis in cancer cells by targeting thioredoxin reductase. *Metallomics* **2014**, *6* (8), 1480−1490.
(67) Lai, H.; Zhao, Z.; Li, L.; Zheng, W.; Chen, T. Antiangiogenic ruthenium(II) benzimidazole complexes, structure-based activation of distinct signaling pathways. *Metallomics* **2015**, *7* (3), 439−447.
(68) Chu, B.; Liu, F.; Li, L.; Ding, C.; Chen, K.; Sun, Q.; Shen, Z.; Tan, Y.; Tan, C.; Jiang, Y. A benzimidazole derivative exhibiting antitumor activity blocks EGFR and HER2 activity and upregulates DR5 in breast cancer cells. *Cell Death Dis.* **2015**, *6* (3), e1686.
(69) Keri, R. S.; Hiremathad, A.; Budagumpi, S.; Nagaraja, B. M. Comprehensive Review in Current Developments of Benzimidazole-Based Medicinal Chemistry. *Chem. Biol. Drug Des.* **2015**, *86* (1), 19−65.
(70) Tahlan, S.; Kumar, S.; Kakkar, S.; Narasimhan, B. Benzimidazole scaffolds as promising antiproliferative agents: a review. *BMC Chem.* **2019**, *13* (1), 1−16.

https://doi.org/10.1021/acs.inorgchem.1c02979
Inorg. Chem. 2021, 60, 18379−18394

(71) Gaba, M.; Singh, S.; Mohan, C. Benzimidazole: An emerging scaffold for analgesic and anti-inflammatory agents. *Eur. J. Med. Chem.* **2014**, *76*, 494−505.
(72) Karrouchi, K.; Radi, S.; Ramli, Y.; Taoufik, J.; Mabkhot, Y. N.; Al-aizari, F. A.; Ansar, M. h. Synthesis and pharmacological activities of pyrazole derivatives: a review. *Molecules* **2018**, *23* (1), 134.
(73) Ansari, A.; Ali, A.; Asif, M.; Shamsuzzaman. Review: biologically active pyrazole derivatives. *New J. Chem.* **2017**, *41* (1), 16−41.
(74) Akhtar, M. J.; Yar, M. S.; Sharma, V. K.; Khan, A. A.; Ali, Z.; Haider, M. R.; Pathak, A. Recent Progress of Benzimidazole Hybrids for Anticancer Potential. *Curr. Med. Chem.* **2020**, *27* (35), 5970−6014.
(75) Shin, J. M.; Sachs, G.; Cho, Y.-m.; Garst, M. 1-arylsulfonyl-2-(pyridylmethylsulfinyl) benzimidazoles as new proton pump inhibitor prodrugs. *Molecules* **2009**, *14* (12), 5247−5280.
(76) Perrin, D. D.; Armarego, W. L. F. *Purification of Laboratory Chemicals*, 3rd ed.; Pergamon Press: Oxford, U.K., 1988; p 391 pp.
(77) Bennett, M. A.; Huang, T. N.; Matheson, T. W.; Smith, A. K. (η^6-Hexamethylbenzene)ruthenium complexes. *Inorg. Synth.* **1982**, *21*, 74−8.
(78) Sheldrick, G. M. Crystal structure refinement with SHELXL. *Acta Crystallogr., Sect. C: Struct. Chem.* **2015**, *71* (1), 3−8.
(79) Dolomanov, O. V.; Bourhis, L. J.; Gildea, R. J.; Howard, J. A. K.; Puschmann, H. OLEX2: a complete structure solution, refinement and analysis program. *J. Appl. Crystallogr.* **2009**, *42* (2), 339−341.
(80) Seratte, J.; Fulton, R.; Nalley, E. A.; Karcher, A. Estimation of partition coefficients via HPLC and shake flask techniques. *Abstracts of Papers, 223rd ACS National Meeting, Orlando, FL, United States, April 7−11, 2002* 2002, CHED-225.
(81) Hall, M. D.; Telma, K. A.; Chang, K.-E.; Lee, T. D.; Madigan, J. P.; Lloyd, J. R.; Goldlust, I. S.; Hoeschele, J. D.; Gottesman, M. M. Say No to DMSO: Dimethylsulfoxide Inactivates Cisplatin, Carboplatin, and Other Platinum Complexes. *Cancer Res.* **2014**, *74* (14), 3913−3922.
(82) Kumar, B. N. P.; Rajput, S.; Dey, K. K.; Parekh, A.; Das, S.; Mazumdar, A.; Mandal, M. Celecoxib alleviates tamoxifen-instigated angiogenic effects by ROS-dependent VEGF/VEGFR2 autocrine signaling. *BMC Cancer* **2013**, *13*, 273.
(83) Wang, B.; Shen, J.; Wang, Z.; Liu, J.; Ning, Z.; Hu, M. Isomangiferin, a Novel Potent Vascular Endothelial Growth Factor Receptor 2 Kinase Inhibitor, Suppresses Breast Cancer Growth, Metastasis and Angiogenesis. *J. Breast Cancer* **2018**, *21* (1), 11−20.
(84) Deng, X.; Roessler, A.; Brdar, I.; Faessler, R.; Wu, J.; Sales, Z. S.; Mani, N. S. Direct, metal-free amination of heterocyclic amides/ureas with NH-heterocycles and N-substituted anilines in POCl3. *J. Org. Chem.* **2011**, *76* (20), 8262−8269.
(85) Deng, J.; Li, N.; Liu, H.; Zuo, Z.; Liew, O. W.; Xu, W.; Chen, G.; Tong, X.; Tang, W.; Zhu, J.; Zuo, J.; Jiang, H.; Yang, C.-G.; Li, J.; Zhu, W. Discovery of Novel Small Molecule Inhibitors of Dengue Viral NS2B-NS3 Protease Using Virtual Screening and Scaffold Hopping. *J. Med. Chem.* **2012**, *55* (14), 6278−6293.
(86) Kilchmann, F.; Marcaida, M. J.; Kotak, S.; Schick, T.; Boss, S. D.; Awale, M.; Gonczy, P.; Reymond, J.-L. Discovery of a Selective Aurora A Kinase Inhibitor by Virtual Screening. *J. Med. Chem.* **2016**, *59* (15), 7188−7211.
(87) Ortega, J. A.; Arencibia, J. M.; La Sala, G.; Borgogno, M.; Bauer, I.; Bono, L.; Braccia, C.; Armirotti, A.; Girotto, S.; Ganesan, A.; De Vivo, M. Pharmacophore Identification and Scaffold Exploration to Discover Novel, Potent, and Chemically Stable Inhibitors of Acid Ceramidase in Melanoma Cells. *J. Med. Chem.* **2017**, *60* (13), 5800−5815.
(88) Mukherjee, A.; Acharya, S.; Purkait, K.; Chakraborty, K.; Bhattacharjee, A.; Mukherjee, A. Effect of N,N Coordination and RuII Halide Bond in Enhancing Selective Toxicity of a Tyramine-Based RuII (p-Cymene) Complex. *Inorg. Chem.* **2020**, *59* (9), 6581−6594.
(89) Romero-Canelón, I.; Salassa, L.; Sadler, P. J. The Contrasting Activity of Iodido versus Chlorido Ruthenium and Osmium Arene Azo- and Imino-pyridine Anticancer Complexes: Control of Cell Selectivity, Cross-Resistance, p53 Dependence, and Apoptosis Pathway. *J. Med. Chem.* **2013**, *56* (3), 1291−1300.
(90) Pizarro, A. M.; Melchart, M.; Habtemariam, A.; Salassa, L.; Fabbiani, F. P. A.; Parsons, S.; Sadler, P. J. Controlling the Reactivity of Ruthenium(II) Arene Complexes by Tether Ring-Opening. *Inorg. Chem.* **2010**, *49* (7), 3310−3319.
(91) Reithofer, M. R.; Bytzek, A. K.; Valiahdi, S. M.; Kowol, C. R.; Groessl, M.; Hartinger, C. G.; Jakupec, M. A.; Galanski, M.; Keppler, B. K. Tuning of lipophilicity and cytotoxic potency by structural variation of anticancer platinum(IV) complexes. *J. Inorg. Biochem.* **2011**, *105* (1), 46−51.
(92) Wenlock, M. C.; Potter, T.; Barton, P.; Austin, R. P. A Method for Measuring the Lipophilicity of Compounds in Mixtures of 10. *J. Biomol. Screening* **2011**, *16* (3), 348−355.
(93) Maji, M.; Acharya, S.; Bhattacharya, I.; Gupta, A.; Mukherjee, A. Effect of an Imidazole-Containing Schiff Base of an Aromatic Sulfonamide on the Cytotoxic Efficacy of N,N-Coordinated Half-Sandwich Ruthenium(II) p-Cymene Complexes. *Inorg. Chem.* **2021**, *60* (7), 4744−4754.
(94) Gopalakrishna, R.; Gundimeda, U.; Fontana, J.; Clarke, R. Differential distribution of protein phosphatase 2A in human breast carcinoma cell lines and its relation to estrogen receptor status. *Cancer Lett.* **1999**, *136* (2), 143−151.
(95) Morante, Z.; De la Cruz Ku, G. A.; Enriquez, D.; Saavedra, A.; Luján, M.; Luque, R.; Eyzaguirre, E.; Guardamino, D.; Valcárcel, B.; Araujo, J. M.; Pinto, J.; Fuentes, H. A.; Neciosup, S. P.; Gomez, H. L. Post-recurrence survival in triple negative breast cancer. *J. Clin. Oncol.* **2018**, *36*, e13120−e13120.
(96) Petrelli, F.; Barni, S.; Bregni, G.; de Braud, F.; Di Cosimo, S. Platinum salts in advanced breast cancer: a systematic review and meta-analysis of randomized clinical trials. *Breast Cancer Res. Treat.* **2016**, *160* (3), 425−437.
(97) Parveen, S.; Arjmand, F.; Tabassum, S. Development and future prospects of selective organometallic compounds as anticancer drug candidates exhibiting novel modes of action. *Eur. J. Med. Chem.* **2019**, *175*, 269−286.
(98) Martinez-Alonso, M.; Busto, N.; Jalon, F. A.; Manzano, B. R.; Leal, J. M.; Rodriguez, A. M.; Garcia, B.; Espino, G. Derivation of Structure-Activity Relationships from the Anticancer Properties of Ruthenium(II) Arene Complexes with 2-Aryldiazole Ligands. *Inorg. Chem.* **2014**, *53* (20), 11274−11288.
(99) Dellinger, M. T.; Brekken, R. A. Phosphorylation of Akt and ERK1/2 is required for VEGF-A/VEGFR2-induced proliferation and migration of lymphatic endothelium. *PLoS One* **2011**, *6* (12), e28947.
(100) Simons, M.; Gordon, E.; Claesson-Welsh, L. Mechanisms and regulation of endothelial VEGF receptor signalling. *Nat. Rev. Mol. Cell Biol.* **2016**, *17* (10), 611−625.
(101) Scartozzi, M.; Bearzi, I.; Berardi, R.; Mandolesi, A.; Pierantoni, C.; Cascinu, S. Epidermal growth factor receptor (EGFR) down-stream signalling pathway in primary colorectal tumors and related metastatic sites: optimizing EGFR-targeted treatment options. *Br. J. Cancer* **2007**, *97* (1), 92−97.
(102) Yoshida, T.; Okamoto, I.; Okabe, T.; Iwasa, T.; Satoh, T.; Nishio, K.; Fukuoka, M.; Nakagawa, K. Matuzumab and cetuximab activate the epidermal growth factor receptor but fail to trigger downstream signaling by Akt or Erk. *Int. J. Cancer* **2008**, *122* (7), 1530−1538.
(103) Ellertsdóttir, E.; Lenard, A.; Blum, Y.; Krudewig, A.; Herwig, L.; Affolter, M.; Belting, H.-G. Vascular morphogenesis in the zebrafish embryo. *Dev. Biol.* **2010**, *341* (1), 56−65.
(104) Lawson, N. D.; Weinstein, B. M. In Vivo Imaging of Embryonic Vascular Development Using Transgenic Zebrafish. *Dev. Biol.* **2002**, *248* (2), 307−318.

https://doi.org/10.1021/acs.inorgchem.1c02979
Inorg. Chem. 2021, 60, 18379−18394